

Photogrammetry for Non-Invasive Terrestrial Position/Velocity Measurement of High-Flying Aircraft

Part II: Direct-Drive Motors

James A Crawford

Synopsis

Part I provided a simple introduction to the big-picture objectives for this multi-phase project. In this project installment, we will begin looking at the servo motor and associated electronic controls. As developed in Part I, pointing repeatability on the order of 10 arc-seconds is the ideal objective. Angular step size can be appreciably larger, but accurate repeatability is a must-have.

The telescope mounts must themselves be precise and rigid, but pointing repeatability and accuracy also depend upon precise servo mechanisms. Closed-loop servo systems are capable of much better performance than open-loop systems which are typically based upon stepper motors and gear/belt reduction schemes. One beautiful aspect of the closed-loop systems is that they can help mitigate scope-wander when light winds would otherwise buffet the telescope ever so slightly.

The signal processing description given in Part I was purposely very brief as it will be separately developed in later project installments. Since the signal processing will combine airplane flight dynamics together with the noise aspects of the real-world measurements, the final results are expected to be better than what the precision limitations of the telescope mount / servo system stand alone would suggest.

Key words that pertain to Part II include direct-drive motor, permanent magnet synchronous motor (PMSM), optical encoder, magnetic encoder, control law, and torque motor. There is a wealth of information on the Internet concerning these different topics, but achieving the performance objectives without breaking the bank will be a major challenge.

1 Getting Started

Getting started primarily entails creating the required hardware platform(s) for collecting pristine image data for subsequent image and related trajectory analysis. This task in and of itself is substantial, involving a very rigid telescope mount and precision motion control. Many different types of telescope mounts can be considered, but astronomical applications are almost always of an equatorial variety which makes the German equatorial mount shown in Figure 1 a favorite choice for that realm. Traditional telescope mounts have frequently made use of worm wheels and worm drives (e.g., Figure 2 and Figure 3) for precise angular control of a telescope mount's axes (e.g., azimuth and elevation, Right Ascension and Declination) whereas this project will be built around more modern state-of-the-art techniques; more specifically, direct-drive motors.

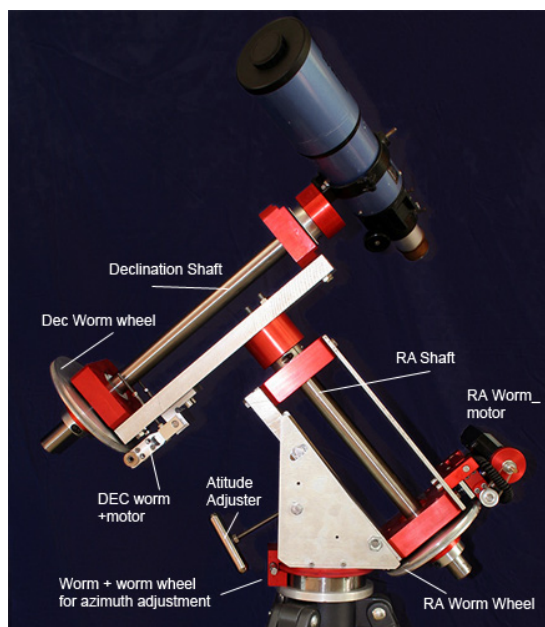


Figure 1 Representative German equatorial telescope mount using worm wheels and gears for the right-ascension and declination axes¹



Figure 2 Worm wheel (left) with mating worm gear (right)



Figure 3 Another perspective for a precision worm wheel and worm gear

¹ From <http://astro.neutral.org/homemade-diy-gem-telescope-mount.shtml>

In this photogrammetry project, azimuth-elevation (Az-El) telescope mounting is much better suited than the German equatorial family. Astronomical observations typically involve star-tracking which is tied to the rotation of the earth, but no such paradigm is involved for a general airplane trajectory across the sky. The German mounts also suffer from *load shifts* when the pointing direction of the telescope crosses the zenith meridian, a problem that is more easily dealt with using Az-El mounts.

A poor-man's view of the Az-El mount is shown here in Figure 4 and Figure 5. The axes are built around two 3-phase permanent magnet washing machine motors from Samsung in large part because of their reasonable cost and multi-pole design (36 poles). Each motor (just the portion shown in Table 1, less axle, bearings, housing, etc.) weighs about 14.4 pounds which is bordering on excessive if portability were an issue. However, additional mass is actually good for overall system rigidity and is consequently viewed in a more positive light here.

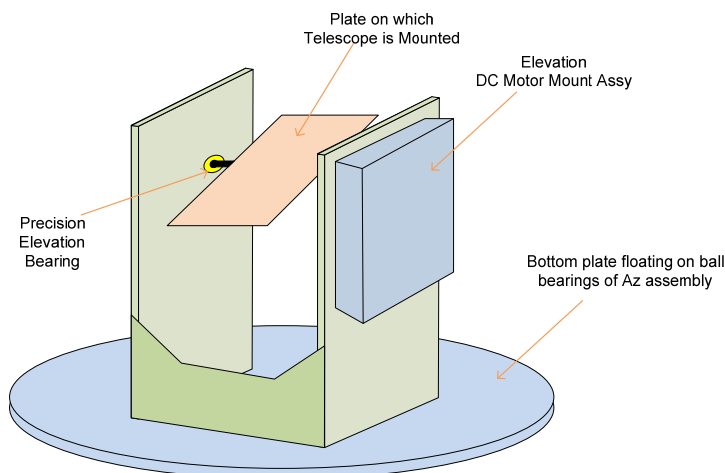


Figure 4 Elevation assembly which is to ride atop the azimuth assembly in Figure 5

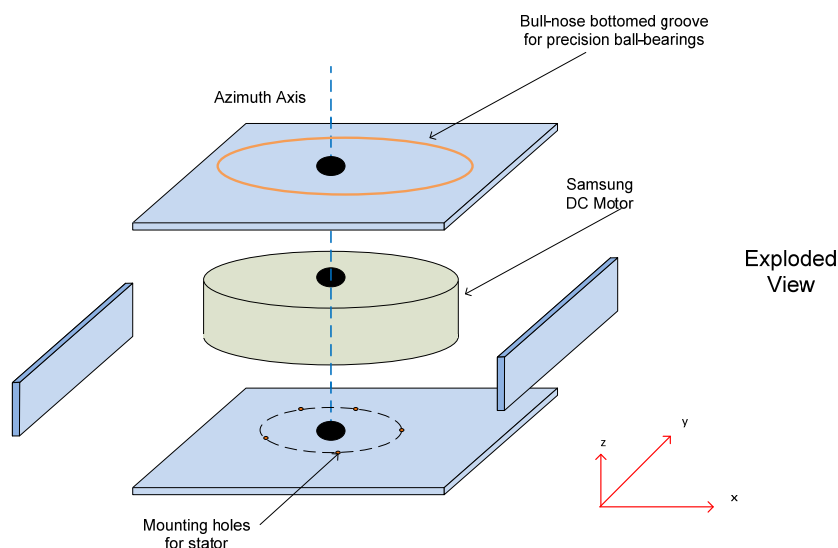


Figure 5 Poor-man sketch of the azimuth assembly. Not shown on the under-side of the bottom plate are three leveling bolts.

Part II is primarily focused on the direct-drive motors required for the Az-El telescope mount. The motors are integrated directly into the mount and the motor bearings are synonymous with the axis bearings of the mount itself. For additional context, an excellent discussion of the topics and solutions that

may be encountered can be found in [7] and some familiarization with this report is encouraged. A sketch of the azimuth-elevation gimbal system used in [7] is shown in Figure 6.

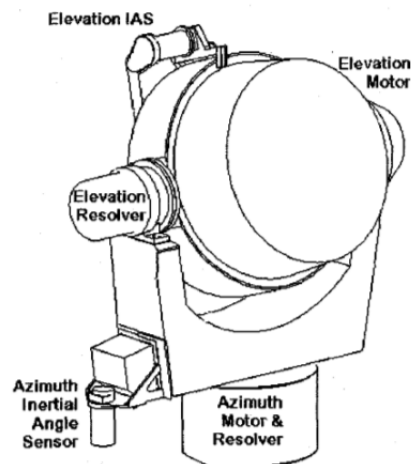


Figure 6 Azimuth-elevation telescope gimbal configuration used in [7]

1.1 Additional Project Context

Completion of the Az-EI telescope mounts will require a substantial amount of effort including:

- Fabrication of rotor/stator housings
- Assembly of the Azimuth direct-drive motor with the Elevation direct-drive motor to form the complete mount as sketched in Figure 4
- Direct-drive motor characterization and modeling
- Development of control law details for controlling the direct-drive motors
- Implementation of control law mathematics into Texas Instruments DSP and associated 3-phase electronics

Once the Az-EI telescope mounts have been designed and built, attention will be focused on the telescope optics and associated CCD imagers. This step will entail some optical work, but also a considerable amount of image processing and tracking.

The complete project will entail building two separate telescopes and situating them on my property (about 300 yard separation). Wireless controls will have to be sorted out along with along real-time back-haul of the image data for subsequent processing. I already have Wifi link and Arduino working in this regard. Precision alignment of the two telescopes is planned to be done against the night-time sky thereby recording any residual pointing errors or misalignment between the two telescopes that may arise.

2 Direct-Drive Motors

Permanent magnet synchronous motors (PMSM) using sinusoidal 3-phase drive have been selected for this project. Other choices are certainly possible, but this path married with vector control (also termed *field oriented control* FOC by others) represents the present state-of-the-art for high efficiency and constant torque performance. The direct-drive motor path has been selected in part based upon the astronomical goals identified in [4]:

1. Completely eliminate all backlash
2. Completely eliminate all periodic error (typically associated with worm drive or friction drive methods)
3. Completely eliminate all non-periodic error
4. Adopt a closed-loop system approach (with feedback) rather than the traditional open-loop methods thereby being able to counteract small gusts of wind or load-shifting related imperfections
5. Deliver smooth slewing rates, up to 45° per second if desired

The direct-drive approach is one of the few closed-loop control system approaches that can be used. It is very attractive in part because control systems and mathematics are used to counter most of the mechanical imprecisions (as well as mechanical wear at some point) present in the hardware.

2.1 Direct-Drive Motor Preliminaries

The direct-drive motors used in this project consist of several key ingredients:

- Digital signal processor for computing real-time motor drive signal solutions
- High current/voltage motor drive electronics
- Precision rotary encoder
- 3-phase sinusoid driven direct motor

In 2011, Cheng and Yuan [1] performed a very helpful cursory examination of the different digital signal processing evaluation boards that could be suitable for their induction motor thesis. Their tabular results are provided in Table 2. For reasons given in their thesis, they opted to choose the TMS320F28xx signal processing device from Texas Instruments for their endeavor. Since the list in was not exhaustive in 2011 and market offerings have certainly changed since 2011, it could be worthwhile to survey the marketplace again.

However, cost and user preference will most likely rule the day when it comes to final processor choice thereby making it more valuable to simply enumerate the key features needed in the controller hardware. Note that one of the earlier investigations into telescope direct-drives described in [4] (2008) made use of a fairly plain 96 MHz C8051 microprocessor a precision motor controller. This 8-bit microprocessor does not begin to compare with more modern 32-bit digital signal processors which have integrated floating-point capabilities (e.g., TMS320F28xx), let alone a large amount of support software and design tools.

The desirable characteristics identified for the evaluation board electronics are lifted directly from [1] (with only a few grammatical changes) as follows:

Compulsory:






- **4 ADC Input Channels-** Three inputs for 3-phase current measurement respectively, one for DC link voltage. More channels are preferable, for example, one channel for sampling a speed signal from a tachometer, if used.

- **3-phase PWM-** Three pairs of PWM outputs that can be synchronized with each other, with a switching frequency of 10kHz. The PWM should have sufficient resolution. Additionally, it should be possible to synchronize the A/D conversion with the carrier wave of the PWM.
- **Interface of incremental encoder-** Specific encoder module or external event capture.
- **On-board programming-** Emulator is a superior solution for programming, debug and download.
- **Cost-** High performance-price ratio is desirable.

Optional:

- **CPU computation capability-** As almost all the quantities in vector control are decimals, a microprocessor with a floating-point unit is highly recommended. The differences between fixed-point and floating-point DSP can be substantial.
- **Math function library-** Some DSP manufactures may provide highly-optimized math function, such as $\sin()$ and $\tan()$, in libraries, which can improve code execution efficiency.
- **Available program example-** A set of mature example codes can contribute to the design.
- **Communication interface-** It is an advantage to have USB and CAN interfaces on the board for other applications.
- **DAC output-** It can be used for debugging and to send signals to other devices.

Table 1 Main Components for Direct-Drive Motor Prototype

Computation Engine:	Texas Instruments LAUNCHXL-F28379D		\$35.09
Motor Drive:	Texas Instruments BOOSTXL-DRV8301		\$50.88
Direct-Drive Motor:	Samsung Washing Machine Motor DC31-00111A (Stator), DC31-00112A (Rotor)		\$40.00 (Used)
Precision Encoder:	Avago AEAT-9000-1GH1		\$58.26
Precision Code Wheel:	Avago HEDG-9000-H14		\$34.09

After some independent investigation, I have chosen the motor control family from Texas Instruments for this project, and have selected the hardware elements shown in Table 1 for my first direct-drive motor prototype effort (Digikey pricing).

The total component cost in Table 1 amounts to \$218.32 which is not insignificant when two setups are required per telescope mount, but this cost is still attractive compared to most worm-wheel alternatives. Design and fabrication of a custom streamlined circuit board would likely save an appreciable amount of money if ultimately desired. A 24V power source will likely be required for the motor, but the details will have to be assessed once more is known about the direct-drive motor itself.

The Avago encoder choice limits the angular precision to 17-bits (about 9.89 seconds of arc). While this precision is adequate for the photogrammetry project as planned, it would be insufficient for a high-quality astronomical telescope where sub-arc-second precision is really needed (24-bit precision would theoretically be 0.077 seconds of arc). Higher encoder precision encoders are available (e.g., Renishaw, Posic), but at substantially higher cost.

2.2 Mechanical Hardware Design

Reverse engineering of the Samsung motor's physical parameters turned out to be fairly time consuming since the air-gap between the stator and rotator is only about $1/16^{\text{th}}$ of an inch (see Figure 7) and good alignment is critical. The outside diameter of the rotator is about 12 inches. Rather than attempt to mate with the center bushing of the rotator, I decided to make use of the three center mounting holes and plastic rib structure for attachment of the rotator to the axle. Details for the Samsung stator/rotator are shown in Figure 8 through Figure 11 whereas details for fabrication of the central mounting hub are shown in Figure 12 through Figure 16.

At the time, I did not have my new Haas TM-1P milling machine (see Figure 42) on line yet so the center hub shown in Figure 13 and Figure 14 was cut from 1" thick Azek planking material² I had on hand using my CNC router (see Figure 40).

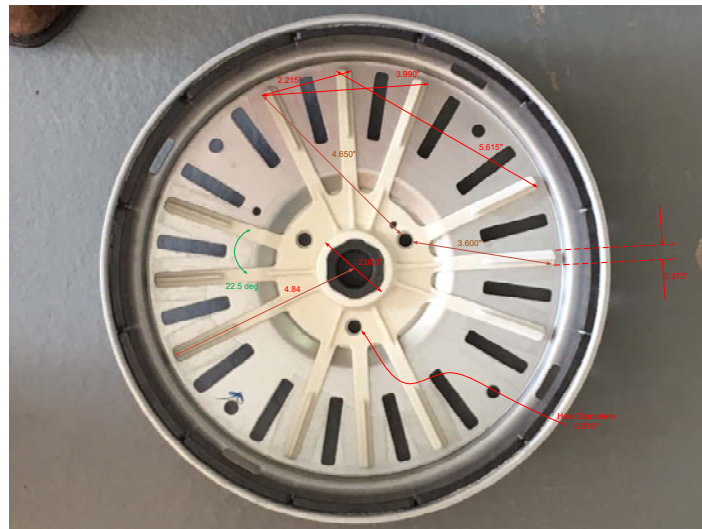


Figure 7 Bottom view of rotor³

² Typically used for exterior porch decking.

³ From U25073 Photogrammetry Part II Figures.vsd.

Table 2 Motor Controller Evaluation Board Candidates⁴

No.	Evaluation Board Manufacturer	CPU Type	System Frequency	3-phase PWM No. of Channels Max. Resolution @Max. Counter Freq.	ADC No. of Channels Max. Resolution @Max. Sampling Freq. Or Min. Conversion Time	ADC&PWM Synchronized	DAC	Event Capture External Interrupt	Encoder Module	CAN	USB	JTAG in which way?	Emulator included	Math Library	Price
1	56F8037EVM Freescale	16-bit Fixed-point	32MHz	6-channel 15-bit @96MHz	2*8 Channels 12-bit @2.67MSPS	Yes	12-bit 2 Channels	Yes	Quadrature Counter*2	Yes	No	Yes by USB	Yes	Yes	\$199.1
http://www.freescale.com/webapp/sps/site/prod_summary.jsp?code=MC56F8037EVM&fsrc=1															
2	56F8367EVM Freescale	16-bit Fixed-point	60MHz	6-channel*2 15-bit @60MHz	4*4 Channels 12-bit @5MSPS	Yes	No	Yes	Quadrature Decoder*2	Yes	No	Yes by Parallel port	Yes	Yes	\$299.1
http://www.freescale.com/webapp/sps/site/prod_summary.jsp?code=MC56F8367EVM&fsrc=1															
3	TMS320F28335 Experimenter Kit Texas Instruments	32-bit Floating-point	150MHz	6-channel*2 16-bit @150MHz	2*8 Channels 12-bit @80ns	Yes	No	Yes	Quadrature Decoder*2	Yes	No	Yes by USB	Yes	Yes	\$99
http://focus.ti.com/docs/toolsw/folders/print/tmsd28335.html															
4	TMS320C28346 ControlCARD Texas Instruments	32-bit Floating-point	300MHz	6-channel*3 16-bit @300MHz	No	Yes with external ADC	No	Yes	Quadrature Decoder*3	Yes	No	Yes by USB	No	Yes	\$125
http://focus.ti.com/docs/prod/folders/print/tms320c28346.html															
5	Easy Kit XC878 Infineon	8-bit MCU+ 16-bit vector computer	24MHz	6-channel 16-bit @24MHz	8 Channels 10-bit @200ns	Yes	No	Yes	No	Yes	No	Yes by USB	No	No	€99
http://www.infineon.com/dgdl/Microcontroller-XC87x-Data-Sheet-V15-infineon.pdf?folderId=db3a304412b407950112b40c497b0af6&fileId=db3a30432239cccd01231293d56908b1															
6	ADZS-BF506F EZ-KIT Lite Analog Devices	16-bit*2 Fixed-point	400MHz	6-channel*2 16-bit @400MHz	2*6 Channels 12-bit @2MSPS	Yes	No	Yes	No	Yes	No	Yes by USB	No	No	\$199
http://www.analog.com/en/embedded-processing-dsp/blackfin/BF506-HARDWARE/processors/product.html															
7	ST7MC control board STMicroelectronics	8-bit MCU	83MHz	6-channel 8-bit @83MHz	1*16 Channels 10-bit @3.5us	N/A	No	Yes	No	No	No	No	No	No	\$96.36
http://www.st.com/Internet/mcu/product/117672.jsp															
8	Explorer 16 Starter Kit Microchip	16-bit Fixed-point	40MHz	6-channel 16-bit @40MHz	2*16 Channels 12-bit @0.5MSPS	Yes	No	Yes	Quadrature Decoder	Yes	No	Yes by USB	Yes	N/A	\$299
http://www.microchip.com/stellent/idcplg?IdcService=SS_GET_PAGE&nodeId=1406&docName=en027853															

⁴ Table 3.3 from [1], 2011.

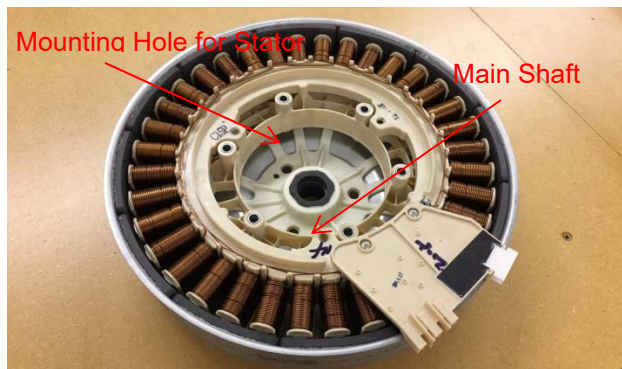


Figure 8 Bottom side of the Samsung DC motor



Figure 9 Top-side of the Samsung DC motor showing only the rotator

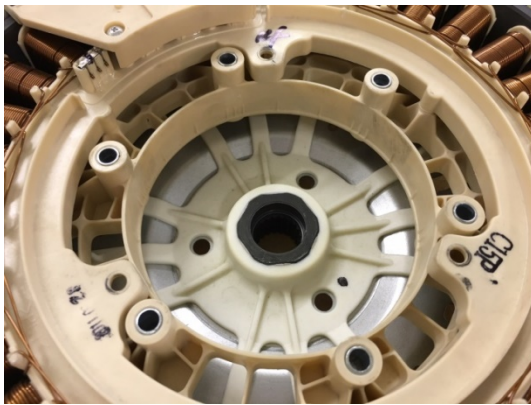


Figure 10 Close-up of Figure 8



Figure 11 Close-up of Figure 9

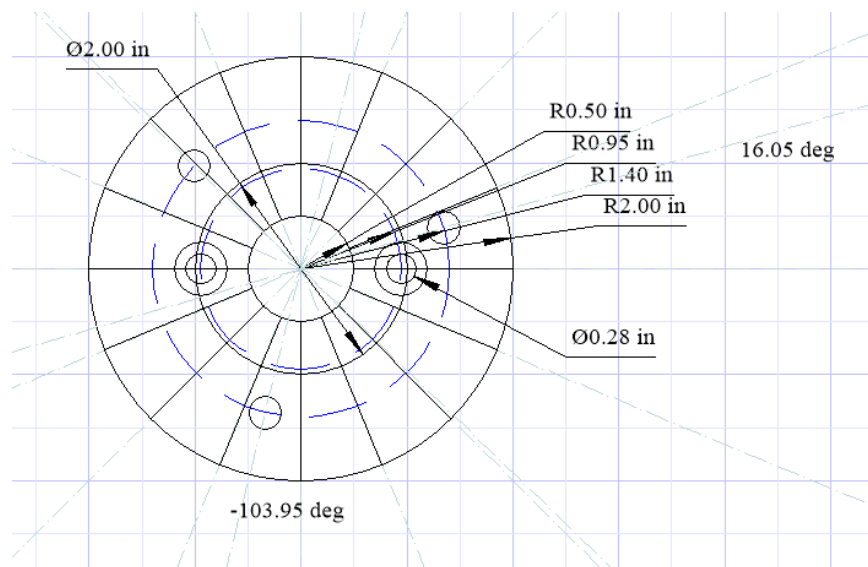


Figure 12 TurboCAD 2-dimensional drawing of coupler disk shown in Figure 13. The 16 spine radials shown here and in Figure 13 are situated with respect to the three mounting holes such that the disk properly lines up in only one position.



Figure 13 Axle-rotor coupling disk routed using CNC router with Azek plastic. 16 grooves line up with the ribs inside the rotor.



Figure 14 Back side of Figure 13. Plastic material is 1" thick. The 2" circular recess for the axle clamp is 0.43" deep. The counter-sinks for the axle clamp are 0.65" deep.



Figure 15 Coupling disk mounted inside the motor's rotator along with a 20mm axle clamp

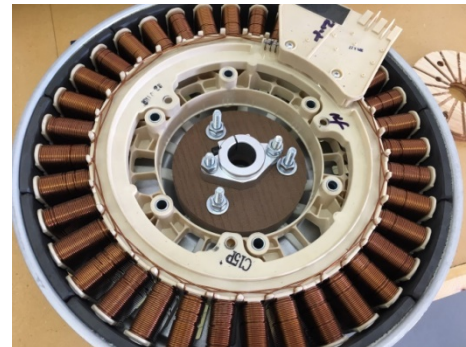


Figure 16 Underside of motor's rotator and stator showing the axle coupling disk. Bolt lengths remain to be trimmed.

Details for the main axle clamps and main axle bearings are provided in Table 3 and Table 4. Most of the materials needed for the azimuth portion of the drive are shown together in Figure 17. Notable exceptions include (i) the three feet which will be attached to the bottom plate and serve as a mechanical interface to a 3-legged tripod or cement pier and (ii) the fine adjustment spacer which will mate up between the bottom side of the bottom plate and the precision optical encoder assembly.

All of the new mechanical design has been done using Autodesk's Fusion 360 tool. This software tool provides a complete design flow and can be precisely configured for my Haas TM-1P mill.

Table 3 Main Axle Clamps



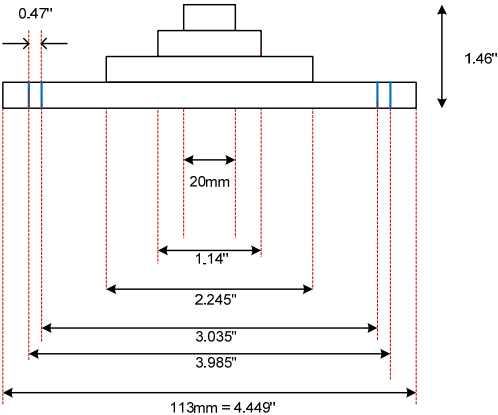
UsongShine SHF20 Linear
Shaft Holder 20mm

https://www.amazon.com/gp/product/B07H4HX7MH/ref=oh_aui_detailpage_o05_s00?ie=UTF8&psc=1

SHF

型号 Designation	轴径 Shaft Diameter	尺寸 Dimensions (mm)							安装螺栓型号 Mounting bolt designation	夹紧螺栓型号 Clamping bolt designation	重量 Weight (gf)
		L	T	F	B	G	H	S			
SHF10	φ 10	43	10	5	32	20	24	5.5	M5	M4	13
SHF12	φ 12	47	13	7	36	25	28	5.5	M5	M4	20
SHF13	φ 13	47	13	7	36	25	28	5.5	M5	M4	20
SHF16	φ 16	50	16	8	40	28	31	5.5	M5	M4	27
SHF20	φ 20	60	20	8	48	34	37	7	M6	M5	40
SHF25	φ 25	70	25	10	56	40	42	7	M6	M5	60
SHF30	φ 30	80	30	12	64	46	50	9	M8	M6	110
SHF35	φ 35	92	35	14	72	50	58	12	M10	M8	380
SHF40	φ 40	102	40	16	80	56	67	12	M10	M10	510
SHF50	φ 50	122	50	19	96	70	83	14	M12	M12	890
SHF60	φ 60	140	60	23	112	82	95	14	M12	M12	1,500

Table 4 Main Axle Bearings⁵ (UCFL204)

		https://www.amazon.com/gp/product/B0769GHSFX/ref=oh_aui_detailpage_o06_s00?ie=UTF8&psc=1 Ucell Block Bearing UCFL204 20mm
		

⁵ From U25073 Photogrammetry Part II Figures.vsd.

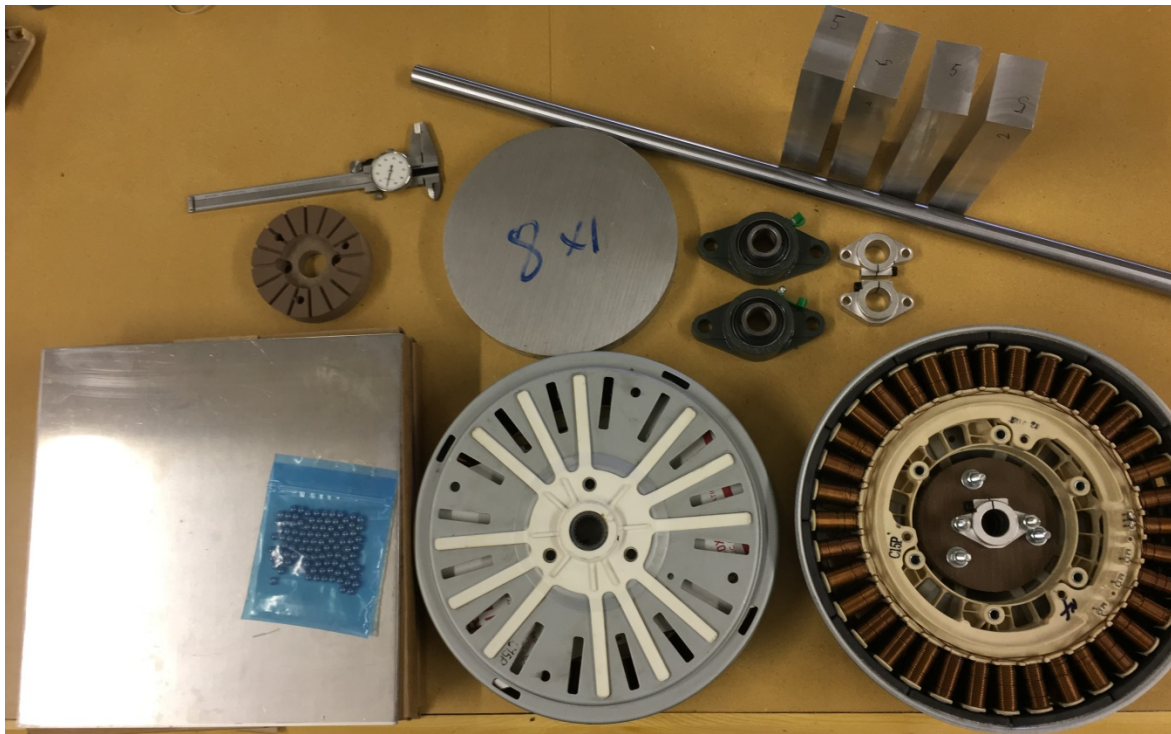


Figure 17 Most of the materials needed for the azimuth drive motor portion. The four rectangular bars in the upper right-hand corner will serve as spacers for the top and bottom plates of the azimuth motor housing. For practice, they were milled to an accuracy of about 0.0005" on all six faces. The 8" aluminum disk will be milled into the azimuth turn-table shown in Figure 4.

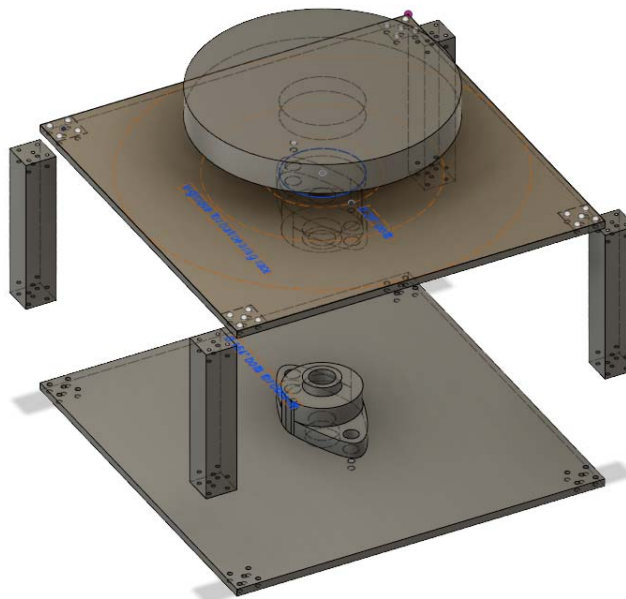


Figure 18 Fusion 360 CAD drawing of the azimuth motor section in progress

There is still a lot of work to be done in order to bring the azimuth portion of the mount together. Next steps are described in §6.1.

3 3-Phase Direct-Drive Motor Control Basics

Three-phase motors make it possible to control shaft rotation and position in a very precise manner. Since the chosen Samsung motor has 36 individual poles, angular position control is made that much easier. The large number of poles should also provide more than enough torque for this application⁶.

The three stator currents are shown as vectors in the time snapshot shown in Figure 19. These vectors rotate with the shaft and magnetic field in a synchronous machine.

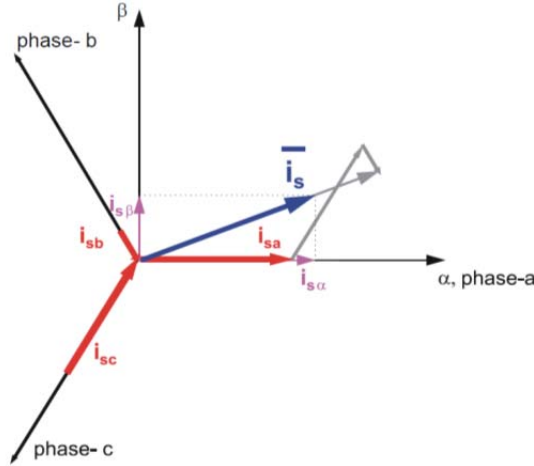


Figure 19 3-phase stator currents i_{sa} , i_{sb} , and i_{sc} along with their 2-dimensional equivalent representation $i_{s\alpha}$ and $i_{s\beta}$

Assuming that i_{sa} , i_{sb} , and i_{sc} are the instantaneous balanced 3-phase stator currents, Kirchoff's current law dictates that

$$i_{sa} + i_{sb} + i_{sc} = 0 \quad (1)$$

The stator current vector \vec{i}_s can be expressed as

$$\vec{i}_s = k(i_{sa} + ai_{sb} + a^2i_{sc}) \quad (2)$$

where $k = 2/3$ and $a = \exp(j2\pi/3)$ from the phase relationships shown in Figure 19. In terms of the 2-axis theory illustrated in Figure 19,

$$\begin{aligned} \vec{i}_s &= i_{s\alpha} + ji_{s\beta} \\ &= k \left[i_{sa} + i_{sb} \cos\left(\frac{2\pi}{3}\right) + i_{sc} \cos\left(\frac{4\pi}{3}\right) \right] + jk \left[i_{sb} \sin\left(\frac{2\pi}{3}\right) + i_{sc} \sin\left(\frac{4\pi}{3}\right) \right] \\ &= k \left[i_{sa} - \frac{1}{2}i_{sb} - \frac{1}{2}i_{sc} \right] + jk \left[\frac{\sqrt{3}}{2}i_{sb} - \frac{\sqrt{3}}{2}i_{sc} \right] \end{aligned} \quad (3)$$

⁶ In the future, this same Samsung motor type may be used for heavier loads in which the additional torque may be required.

⁷ From Figure 2-2 of [3].

In this context, $i_{s\alpha}$ and $i_{s\beta}$ are fictitious in-phase and quadrature-phase currents that simplify the subsequent mathematics substantially. In matrix form, (3) can be rewritten as

$$\begin{bmatrix} i_{s\alpha} \\ i_{s\beta} \end{bmatrix} = k \begin{bmatrix} 1 & -\frac{1}{2} & -\frac{1}{2} \\ 0 & \frac{\sqrt{3}}{2} & -\frac{\sqrt{3}}{2} \end{bmatrix} \begin{bmatrix} i_{sa} \\ i_{sb} \\ i_{sc} \end{bmatrix} \quad (4)$$

with $k = 2/3$. The inverse relationship of (4) is given by

$$\begin{bmatrix} i_{sa} \\ i_{sb} \\ i_{sc} \end{bmatrix} = \begin{bmatrix} \frac{2}{3} & 0 \\ -\frac{1}{3} & \frac{1}{\sqrt{3}} \\ -\frac{1}{3} & -\frac{1}{\sqrt{3}} \end{bmatrix} \begin{bmatrix} i_{s\alpha} \\ i_{s\beta} \end{bmatrix} \quad (5)$$

Identical relationships to (4) and (5) apply for the motor voltages and magnetic fluxes as well. These 2-axis transformations are known as the *Clarke transformation* where (4) is the *forward* transformation and (5) is the *reverse* transformation.

Borrowing from [13] for the applied stator 3-phase voltages,

$$\begin{aligned} u_{sa} &= R_s i_{sa} + \frac{d\Psi_{sa}}{dt} = R_s i_{sa} + \frac{d}{dt}(L_s i_{sa} + \Psi_{Ma}) \\ u_{sb} &= R_s i_{sb} + \frac{d\Psi_{sb}}{dt} = R_s i_{sb} + \frac{d}{dt}(L_s i_{sb} + \Psi_{Mb}) \\ u_{sc} &= R_s i_{sc} + \frac{d\Psi_{sc}}{dt} = R_s i_{sc} + \frac{d}{dt}(L_s i_{sc} + \Psi_{Mc}) \end{aligned} \quad (6)$$

where

u_{sa}, u_{sb}, u_{sc}	individual phase voltages [V]
R_s	stator resistance [Ω]
i_{sa}, i_{sb}, i_{sc}	individual phase currents [A]
$\Psi_{sa}, \Psi_{sb}, \Psi_{sc}$	individual phase magnetic flux [Weber]
$\Psi_{MA}, \Psi_{MB}, \Psi_{MC}$	individual rotor flux [Weber]
L_s	stator inductance [H]

For mathematical torque equilibrium,

$$J \frac{d\omega_{motor}}{dt} = \tau_{driving} - K_f \omega_{motor} - \tau_{load} \quad (7)$$

where

J	moment of load inertia [kg m ²]
ω_{motor}	motor driving torque [Nm]
K_f	viscous coefficient of the load [kg m ² s ⁻¹]
$\tau_{driving}$	motor driving torque [Nm]
τ_{load}	load torque [Nm]

In this context, the quantity $K_f \omega_{motor}$ represents mechanical loss in the system. The motor driving torque is given by

$$\tau_{driving} = \frac{p}{\dot{\omega}_e} \left[\frac{3}{2} \text{Re}(U_s I_s) - 3R_s I_s^2 \right] \quad (8)$$

where

p	number of pole pairs
ω_e	electrical angular speed [rad/s]
U_s	supply voltage [V]
I_s	supply current [A]

In terms of the transformed quantities from using (4),

$$\begin{aligned} u_{s\alpha} &= R_s i_{s\alpha} + L_s \frac{di_{s\alpha}}{dt} - \Psi_M \sin(\theta_e) \omega_e \\ u_{s\beta} &= R_s i_{s\beta} + L_s \frac{di_{s\beta}}{dt} + \Psi_M \cos(\theta_e) \omega_e \\ J \frac{d\omega_e}{dt} &= \frac{3}{2} p^2 \Psi_M [i_{s\beta} \cos(\theta_e) - i_{s\alpha} \sin(\theta_e)] - K_f \omega_e - p \tau_{load} \end{aligned} \quad (9)$$

The *Park transformation* is a second transformation that conveniently simplifies the rotational elements as

$$\begin{bmatrix} i_d \\ i_q \end{bmatrix} = \begin{bmatrix} \cos(\theta_e) & \sin(\theta_e) \\ -\sin(\theta_e) & \cos(\theta_e) \end{bmatrix} \begin{bmatrix} i_{s\alpha} \\ i_{s\beta} \end{bmatrix} \quad (10)$$

where θ_e is the instantaneous electrical angle. For synchronous systems (as here), the speed of the rotating electromagnetic field and rotor are equal. Applying this transformation to (9) produces the key results

$$\begin{aligned} u_d &= R_s i_d + L_s \frac{di_d}{dt} - L_s \omega_e i_q \\ u_q &= R_s i_q + L_s \frac{di_q}{dt} + L_s \omega_e i_d + \Psi_M \omega_e \\ J \frac{d\omega_e}{dt} &= \frac{3}{2} p^2 \Psi_M i_q - K_f \omega_e - p \tau_{load} \end{aligned} \quad (11)$$

These equations can be expressed in state-variable form as⁸

⁸ Equation (32) of [13].

$$\frac{d}{dt} \begin{bmatrix} i_d \\ i_q \\ \omega_e \\ \tau_{load} \end{bmatrix} = \begin{bmatrix} \frac{-R_s}{L_s} & \omega_e & 0 & 0 \\ -\omega_e & \frac{-R_s}{L_s} & \frac{-\Psi_M}{L_s} & 0 \\ 0 & \frac{3p^2}{2J} \Psi_M & \frac{-K_f}{J} & \frac{-p}{J} \\ 0 & 0 & 0 & 0 \end{bmatrix} \begin{bmatrix} i_d \\ i_q \\ \omega_e \\ \tau_{load} \end{bmatrix} + \begin{bmatrix} \frac{1}{L_s} & 0 \\ 0 & \frac{1}{L_s} \\ 0 & 0 \\ 0 & 0 \end{bmatrix} \begin{bmatrix} u_d \\ u_q \end{bmatrix} \quad (12)$$

This result is sufficient for speed-control applications, but modifications are required in the case of angular position control. The modified state-variable result adds in θ_e as

$$\frac{d}{dt} \begin{bmatrix} i_d \\ i_q \\ \omega_e \\ \theta_e \end{bmatrix} = \begin{bmatrix} -\frac{1}{\tau} & 0 & 0 & 0 \\ 0 & -\frac{1}{\tau} & -\frac{\Psi_M}{L} & 0 \\ 0 & \frac{3p^2 \Psi_M}{2J} & -\frac{K_f}{J} & 0 \\ 0 & 0 & 1 & 0 \end{bmatrix} \begin{bmatrix} i_d \\ i_q \\ \omega_e \\ \theta_e \end{bmatrix} + \begin{bmatrix} \frac{u_d}{L} \\ \frac{u_q}{L} \\ -\frac{p}{J} \tau_{load} \\ 0 \end{bmatrix} + \begin{bmatrix} \omega_e i_q \\ -\omega_e i_d \\ 0 \\ 0 \end{bmatrix} \quad (13)$$

where the nonlinear products $\omega_e i_q$ and $\omega_e i_d$ have also been moved to the far-right vector as well. This result has the form

$$\frac{d}{dt} \vec{x} = \vec{A} \vec{x}(t) + \vec{B}(t) \vec{u}(t) + \vec{C}(\vec{x}) \quad (14)$$

In precision positioning applications, vector \vec{C} trends to the all-zero vector since $\omega_e \rightarrow 0$. Designing the control elements around this motor remains to be done.

Thus far, nothing has been said about motor related quantities like its moment of inertia J and its viscous friction coefficient K_f , let alone other real-world complications like cogging. Characterization of the Samsung motor is explored in §3.1.

3.1 Samsung Motor Characterization

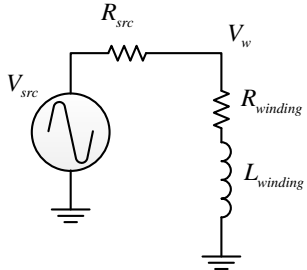
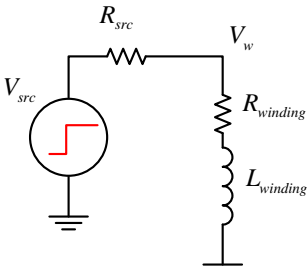
The needed motor modeling parameters were introduced in §3. The motor's stator resistance (per phase) can be found directly using a standard Volt-Ohm meter. I have two Samsung motors on hand with three windings each exhibiting the resistance measurements shown in Table 5.

Table 5 Motor Winding Resistance (Samsung DC31-00111A Stator)

Motor #	Winding 1, Ω	Winding 2, Ω	Winding 3, Ω	Mean, Ω
1	6.0	5.9	6.0	5.97
2	5.75	5.85	5.9	5.83

Stator winding inductance per phase is a bit more complicated to measure. It is best to make this measurement without the rotor present. Each winding can be driven by a low frequency AC source and the winding impedance inferred from the voltage measurement as shown in Figure 20, or a step-voltage

waveform can be applied as shown in Figure 21 and the time constant of the output voltage waveform measured to infer the inductance. Ignoring mutual inductance effects, the motor's stator winding inductance (per phase) could also be measured using a standard RLC meter.

Diagram	Key Equation
 <p>Figure 20 AC source excitation</p>	$V_w = V_{src} \frac{R_{winding} + j\omega L_{winding}}{R_{src} + R_{winding} + j\omega L_{winding}} \quad (15)$
 <p>Figure 21 Step-voltage excitation</p>	$V_w(t) = V_{src} \frac{R_{winding}}{R_{src} + R_{winding}} (1 - e^{-t/\tau})$ $\tau = \frac{L_{winding}}{R_{src} + R_{winding}} \quad (16)$

Beyond these fundamental quantities, this motor is expected to exhibit considerable *cogging torque*. Other nonlinear torque mechanisms will also be present which may or may not pose issues for the project depending upon their severity. There are four main types of torque ripple: mutual, reluctance, cogging, and friction [11].

Mutual torque is caused by the mutual interaction of the rotor's permanent magnets and the stator's currents.

Reluctance torque is a result of variance in the stator's self-inductance due to the rotors magnet saliency.

Cogging torque comes from the rotor's permanent magnets' attraction to the salient portions of the rotor.

Friction torque is not always axially symmetric since motor bearings generally exhibit some eccentricities.

"At very low speeds, torque ripple can cause relatively large speed fluctuations. In servo control, precise positioning is impossible with a traditional proportional or proportional-integral controller due to the ripple's nonlinearity" [11].

Cogging torque ripple is addressed in [11]. It is expected that cogging torque ripple could be an issue for the photogrammetry project, but likely less so for astronomical use where angular velocities are extremely low. It is also expected that torque behavior will be easier to cancel out in an azimuth/elevation mount than in a German equatorial mount.

The rather large number of torque sources, often comingled with nonlinearities, make generation of a torque ripple map difficult. The two torque ripple characterization methods discussed in [11] are (i)

the position-based method and (ii) the acceleration-based method. Each method has its strengths and weaknesses depending upon how the motor is being utilized in a given application.

The initial plan of attack is illustrated in Figure 22 where a mass will be connected to the motor's shaft and measurements made while the mass is allowed to fall. The rotary encoder shown in Table 1 (17-bit precision) will be used to make precision angular measurements of the shaft's motion while the mass is falling and shortly thereafter. Measurements will be made with the stator windings (i) open-circuited, (ii) short-circuited, and (iii) shunted with a fixed resistance values thereby permitting a reasonably good characterization of the motor to be performed. The results and computational details will be presented in Part III of this project series as described in §6.2.

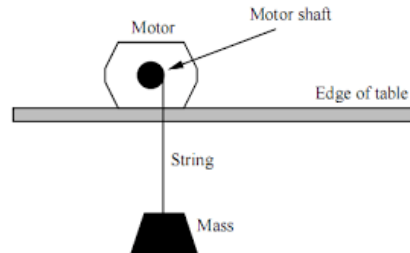


Figure 22 Easy way to measure motor's torque characteristics

4 Motor Control Law

Literature discussions about 3-phase permanent magnet synchronous motors (PMSM) using sinusoidal drive voltages routinely begin with an explanation of the Clarke and Park coordinate transformations such as [2] and [3] from Freescale Semiconductor. Some background material is provided in §10 to connect some of the dots.

Unlike most applications found in the literature, our interest here is primarily for precision telescope pointing in which no sustained rotation is involved. Pointing accuracies better than one arc-second are ultimately desired when an adequately precise angular encoder is employed. The encoder used for this project (AEAT-9000-1GSH0 from Avago Technologies) only exhibits 17-bit absolute accuracy which should make pointing repeatability on the order of $\pm 9.9' / M$ attainable where M is ideally greater than or equal to 4. Even though the encoder resolution is limited to 9.9 seconds of arc, finer servo positional repeatability (i.e., $M > 1$) should be possible by tracking encoder tick transition points in a dithering manner and making use of the mount's inertia to filter out the dither.

The primary issues which will be acutely important for this (potential) portion of the project long-term include:

1. Constrain any limit-cycling to as small a portion of one tick as possible
2. Sufficiently mitigate cogging torque issues
3. Develop adaptive and self-learning techniques as necessary to mitigate systemic errors like slight mis-alignments, eccentricities, etc.
4. Have sufficient dynamic response bandwidth to counter slight wind loading along with adequately low delay when tracking moving objects up to roughly 10° per second.

Once one precision drive has been perfected, it will be duplicated so that an azimuth-elevation telescope mount can be completely assembled.

The baseline plan is to utilize the direct-drive washing machine motor shown in Table 1 as the heart of the precision drive. It so happens that LG Electronics was awarded a patent [6] for a very similar washing machine motor claiming the design "may reduce cogging torque, noise, and vibration." The discussion in [6] is focused upon creating sinusoidal-shaped magnetization patterns rather than the square-wave patterns which are used with brushless DC motors (BLDC), so it is hoped that the direct-drive motor configuration shown in Table 1 will in fact exhibit low cogging torque characteristics.

The azimuth and elevation axes are to be controlled by DC motors as already mentioned. Modeling for the DC motors was developed in §3, but actual control of each motor involves embedding

the motor within a control law framework which is discussed in this section. Hardware implementation of the control law is based upon using the digital signal processor and 3-phase driver hardware introduced in §5. This section provides an introduction into the mathematical aspects of the control law which will be hosted by the TI Launchpad digital signal processor.

Several motor position control algorithms are considered in [12]. It is reported that a state-space based controller exhibited the fastest response and smallest settling time. The state-space model described in [12] is given by

$$\begin{aligned} \frac{d\vec{x}(t)}{dt} &= A\vec{x}(t) + B\vec{u}(t) \\ \vec{y}(t) &= C\vec{x}(t) \end{aligned} \quad (17)$$

where A is the system matrix associates the present system state with changes, B is the control matrix, and C is the output matrix which describes the relationship between the system state and its observed outputs. In this context, equation (13) is a good starting point for the dynamic motor model. This section addresses development of the baseline control law which will be used.

There are many control law approaches reported in the literature, from fairly simple proportional plus integral (PI) controllers to much more complex extended Kalman methods [14], [15] and other adaptive methods. The adopted control law approach can always be made more complex, so the primary motivation here is to adopt an approach having an acceptable amount of performance versus complexity.

Great care must be exercised in redirecting an approach found in the literature for a given problem to other applications where subtle differences end up creating serious (new) problems. As an example of this, the *sliding mode* method of motor control is very intriguing for robust motor control, but it introduces a controllable but nonzero chatter in exchange for outstanding robustness that would likely doom the precision pointing needed in my application.

Since the precision pointing of interest in this project generally involves very slow rotational speed, an *Observer* function is used in the feedback path in order to help circumvent optical encoder's quantization issues while also providing estimates for important quantities like rotational speed. This topic is addressed in the next section.

The PID (proportional, integral, derivative) controller will serve as a baseline approach in §4.2. One flavor of this approach is shown for context in Figure 23. This effort may be followed by a more robust adaptive control method as the need arises.

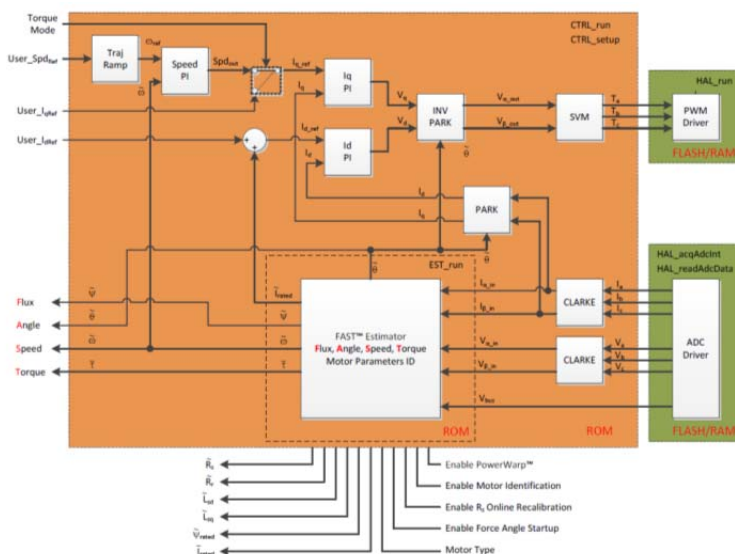


Figure 23 PI controller law used in Texas Instrument's Insta-SPIN⁹

⁹ U25841

4.1 Observer

The optical encoder adopted for this project is identified in Table 1 and provides 17-bit resolution which equates to about 0.002747° or equivalently 9.888 arc-seconds. In the case of static pointing, it is important to avoid chatter and limit-cycle behavior.

An observer is discussed in Dave Wilson's material on field oriented motor control [9] as shown in Figure 24. This filter configuration is also referred to as an *alpha-beta filter* by others and is actually a 2nd-order IIR filter as shown in Figure 25. Modern control system design based upon state-variable techniques routinely utilize the observer concept and relevant material is widely available.

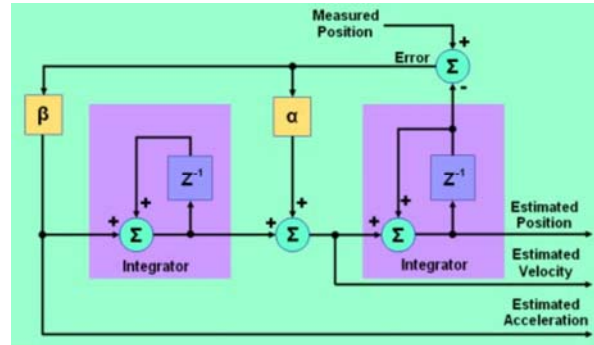


Figure 24 Observer by Dave Wilson [9] for use with an optical encoder, recast as a 2nd order IIR filter in Figure 25

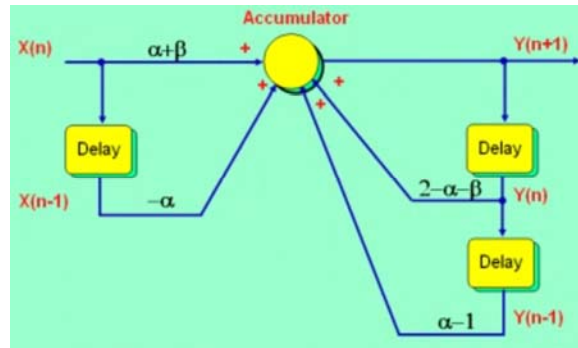


Figure 25 Alpha-beta filter of Figure 24 recast as a second-order IIR filter [9]

The transfer function between estimated position $Y(n)$ and input position $X(n)$ is given by

$$H(z) = X(z) \frac{(\alpha + \beta)z^{-1} - \alpha z^{-2}}{1 + z^{-1}(-2 + \alpha + \beta) + z^{-2}(1 - \alpha)} \quad (18)$$

The α and β values are generally kept small in order to suppress noise. Stability dictates that¹⁰

$$\begin{aligned} 0 < \alpha < 1 \\ 0 < \beta \leq 2 \\ 0 < 4 - 2\alpha - \beta \end{aligned} \quad (19)$$

¹⁰ Wikipedia

Parameter β must be < 1 or else noise will be amplified. These filters have a connection to Kalman filters but this will not be discussed further at this time.

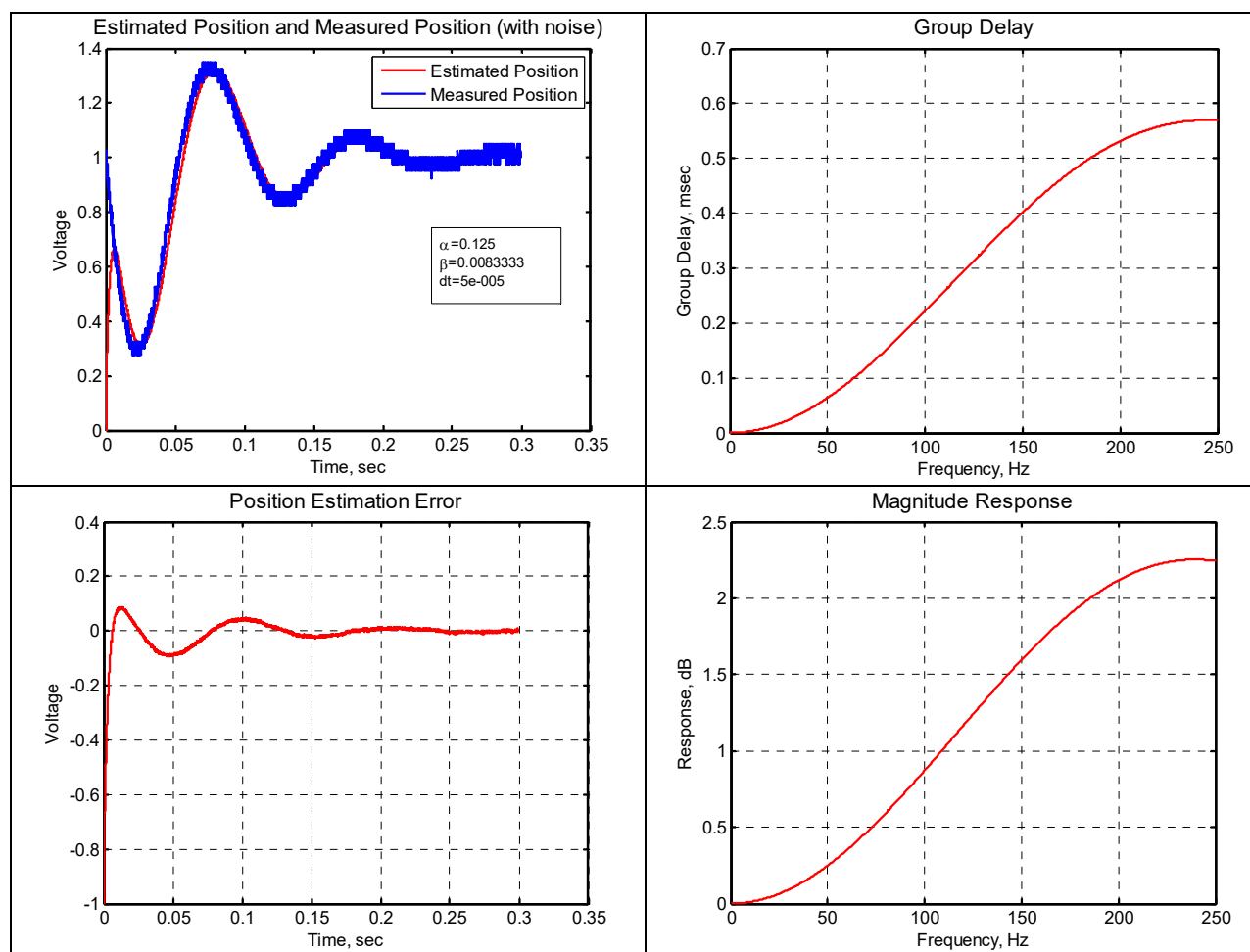
Benedict and Bordner came up with a relationship for β thereby simplifying parameter choices in 1962 [17]. Given a noisy system wherein the desired signal of interest is changing at a constant rate, they stipulated

$$\beta = \frac{\alpha^2}{2 - \alpha} \quad (20)$$

For situations where near-critical damping is desired, they recommended

$$\beta = 0.80 \left[\frac{2 - \alpha^2 - 2\sqrt{1 - \alpha^2}}{\alpha^2} \right] \quad (21)$$

Table 6 Example of Stand-Alone Observer Response to Quantized Damped Sinusoid Input¹¹ Using (20)



A comparison of results for $\alpha = 0.125$ in a system using a sampling rate of 20 ksps, quantization steps of 0.025V and uniformly distributed noise, these two approaches for β -choice are compared in Table 6 and

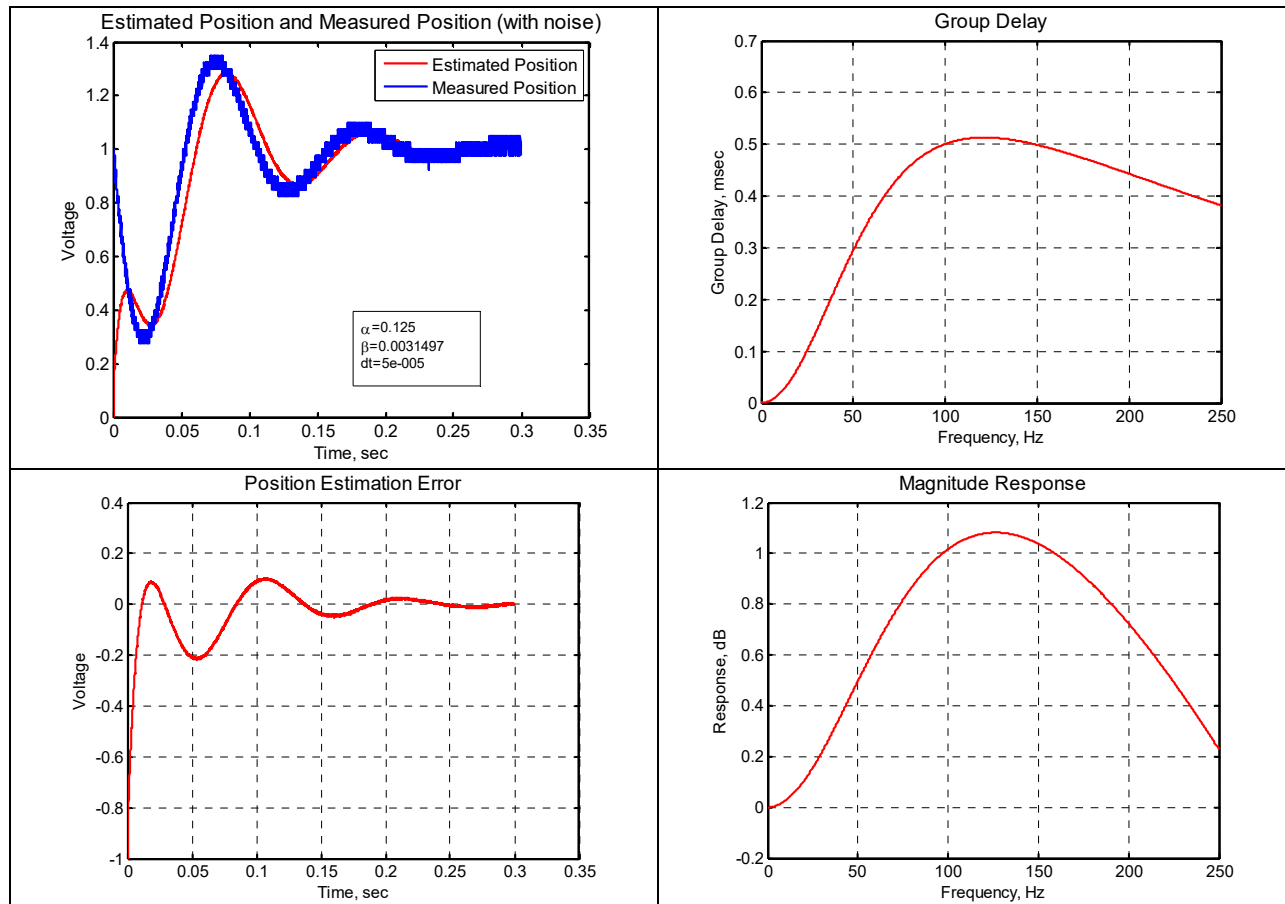
¹¹ Using u25863_tracking_loop.m.

Table 7. Based upon these abbreviated results, the baseline approach will be built around using (20) for now. In the context of Figure 24, the transfer functions of interest are

$$H_{\theta}(z) = \frac{\theta_{est}(z)}{\theta_{meas}(z)} = \frac{(\alpha + \beta) - \alpha z^{-1}}{1 + z^{-1}(\alpha + \beta - 2) + z^{-2}(1 - \alpha)} \quad (22)$$

$$\begin{aligned} H_{\omega}(z) &= \frac{\omega_{est}(z)}{\theta_{meas}(z)} = H_{\theta}(z)(1 - z^{-1}) \\ &= \frac{(\alpha + \beta) - (2\alpha + \beta)z^{-1} + z^{-2}}{1 + z^{-1}(\alpha + \beta - 2) + z^{-2}(1 - \alpha)} \end{aligned} \quad (23)$$

Table 7 Example of Stand-Alone Observer Response to Quantized Damped Sinusoid Input¹² Using (21)



¹² Using u25863_tracking_loop.m.

4.2 PID Control Law

The proportional, integral, derivative (PID) control law is a frequent choice for traditional control system design. A version of this control law incorporating the *Observer* function from §4.1 and the *d-q* motor transformations of §3 is shown in Figure 26. The mathematical model for the motor in *d-q* coordinates (13) developed earlier can be substituted into this block diagram as shown by the dividing line resulting in Figure 27. In Figure 27, the decoupling block is used to transform (u_d, u_q) into (u_d^*, u_q^*) as

$$\begin{aligned} u_d^* &= u_d + \omega_{est} i_q \\ u_q^* &= u_q - \omega_{est} i_d \end{aligned} \quad (24)$$

Since this application is focused on positioning rather than maintaining a constant rotational rate, it's likely that these decoupling terms will be inconsequential because $\omega_{est} \approx 0$ as a rule.

It is early in the project to venture much beyond this introductory discussion about control laws, but understanding what is needed to model the motor itself in §3 is vital in moving the project to its next installment. Nevertheless, some additional discussion is provided in §11.

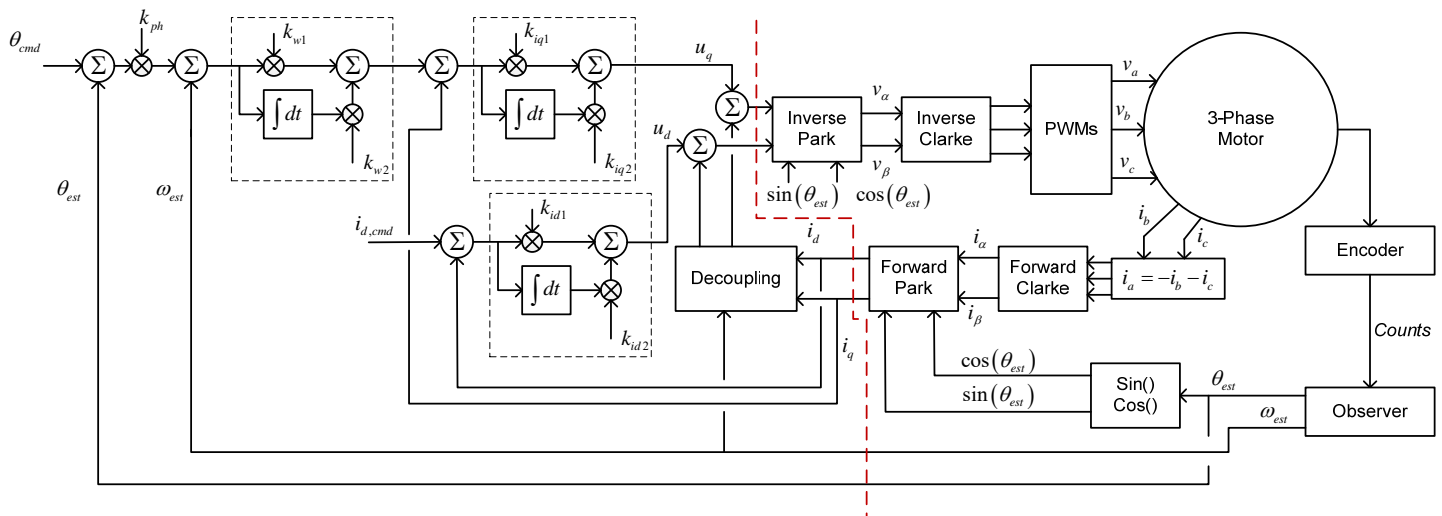


Figure 26 Traditional DC motor control system utilizing proportional-integral (PD) control laws, Clarke-Park transformations, and an Observer¹³. Dashed line shown where mathematical motor model (13) to be substituted in.

¹³ From U25073 Photogrammetry Part II Figures.vsd.

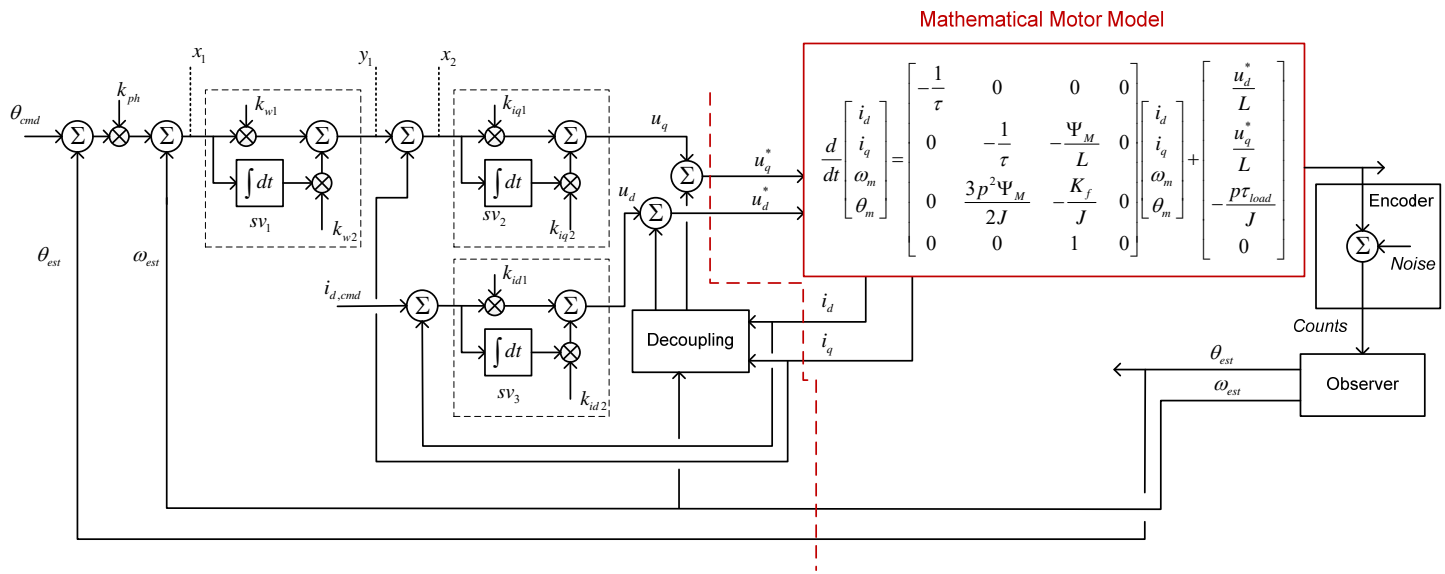


Figure 27 Mathematical model for motor substituted into Figure 26. The observer of Figure 24 contains two state-variables making a total of 9 for the entire system.

5 Direct-Drive Motor Control Using TI's Software

The motor controller I purchased was the LAUNCHXL-F28379D from Texas Instruments (Table 1). To get started, I first downloaded the Code Composer Studio (CCS) from <http://www.ti.com>. This is a fairly massive download entailing more than 1 GB. I enabled the option for the C2000 Microcontroller when I was prompted. I also downloaded the C2000Ware_DigitalPower_SDK from TI as well.

To see that my LAUNCHXL-F28379D hardware was properly functioning, I followed the directions in §5.1 and §5.2 of the “LAUNCHXL-F28379D Overview, User's Guide” [8]. I subsequently launched the PuTTY terminal application program and found everything in working order. Pictures of the TI hardware are shown in Figure 28 and Figure 29 along with my laptop's screen running the PuTTY utility with the F28379D hardware.



Figure 28 Basic LAUNCHXL-F28379D controller board from TI



Figure 29 LAUNCHXL-F28379D controller board with BOOSTXL-DRV8301 piggy-backed on top

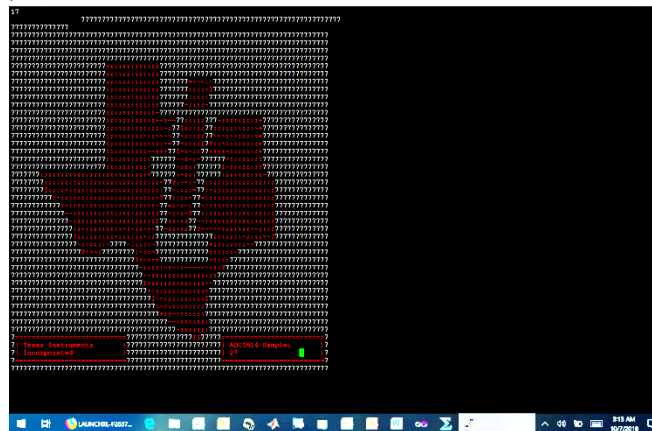


Figure 30 Laptop screen shot running PuTTY with the LAUNCHXL-F28379D cabled up via a USB port

6 Next Steps

This project is multi-faceted and quite involved. But that is what makes it challenging and enjoyable at the same time. My plans for the next installment of the project are discussed in the following sections.

6.1 Mechanical Design

Much of the mechanical design for the azimuth portion of the telescope mount has already been done, but the pieces have yet to be put all together. Much of my time has been spent getting familiar with the new TM-1P mill and associated Fusion 360 design software, but I would not say that I've *arrived* yet! In the case of the TM-1P mill, very powerful servos are used (the moveable table can support workpieces up to 1,000 pounds in weight) so I have been progressing with great care as I'm genuinely a newbie when it comes to a CNC like the TM-1P.

For my next project installment, I plan to have:

- Milled top and bottom plates
- Milled supporting feet (3)
- Milled precision fine-adjustment spacer for the optical encoder
- Assemble the complete azimuth drive motor section

6.2 Motor Characterization

Once the azimuth drive motor section has been assembled, it will be possible to characterize the Samsung DC motor I have selected for the project.

Obtaining electrical quantities for the motor like resistance and inductance should not be difficult as described in §3.1. Obtaining moment of inertia, friction, and cogging torque behavior will be considerably more involved, however,

For my next project installment, I plan to have completed:

- models for motor winding resistance and inductance parameters
- instrumentation setups to capture real-time rotational information from the optical encoder using either the TI DSP or an Arduino Mega
- extract modeling parameters for the control system design
- quantify the magnitude of the potential issues surrounding the cogging torque topic

6.3 Motor Control

Motor control will be predicated upon completing the previous tasks in this section. In addition, however, the following tasks must be accomplished in the next installment in order to have a working azimuth control section:

- develop proficiency with the TI Launchpad programming environment
- refine the mathematical baseline for the motor control algorithm
- modify the baseline algorithm as necessary to achieve stated performance goals

Of the targeted tasks for the next installment of this project, this motor control task will likely be the most time-consuming. There is always a degree of *adventure* anytime theory and hardware come together.

The motor control for this project will be built upon state-variable methods, §11. Much work remains to be done as briefly introduced in §12.

7 References

1. Qian Cheng and Lei Yuan, "Vector Control of an Induction Motor Based on a DSP," Master of Science Thesis, Chalmers University, 2011, U25041.
2. Freescale Semiconductor, "3-Phase PM Synchronous Motor Vector Control Using a 56F80x, 56F8100, or 56F8300 Device," Application Note AN1931, Jan. 2005.
3. _____, "PM Sinusoidal Motor Vector Control with Quadrature Encoder," Sept. 2008, U24984.
4. Dan Gray, "Direct Drive Motors for the Amateur Budget (a work in progress)," 18 May 2008, U24888.
5. David Halliday and Robert Resnick, *Fundamentals of Physics*, John Wiley and Sons, 1970.
6. In Geun Ahn, "Direct Drive Motor for Washing Machine and Method of Manufacturing the Same," US Patent 7,692,349, 6 April 2010.
7. Anthony E. Bentley, "Pointing Control Design for a High Precision Flight Telescope Using Quantitative Feedback Theory," Sandia National Laboratories, 2000, U25096.
8. Texas Instruments, "LAUNCHXL-F28379D Overview, User's Guide," Literature Number SPRUI77A, August 2017, U25038.
9. Dave Wilson, "Field Oriented Control of Permanent Magnet Motors," <https://training.ti.com/field-oriented-control-permanent-magnet-motors?cu=1135458>, U25838.
10. Renesas, "Motor Control Application, Vector Control for Permanent Magnet Synchronous Motor with Encoder," Application Note R01AN3789EJ0101, 7 July 2017, U25829.
11. Matthew Piccoli and Mark Yim, "Cogging Torque Ripple Minimization via Position-Based Characterization," U25085.
12. N. Bacac, V. Slukic, et al., "Comparison of Difference DC Motor Positioning Control Algorithms," *MIPRO 2014*, U24983.
13. Kvetoslav Belda, "Mathematical Modelling and Predictive Control of Permanent Magnet Synchronous Motor Drives," *Trans. Electrical Engineering*, 2013, U25081.
14. D. Lenine, B. Rami Reddy, and S. Vijay Kumar, "Estimation of Speed and Rotor Position of BLDC Motor Using Extended Kalman Filter," *IET-UK International Conference on Information and Communication Technology in Electrical Sciences*, 2007, U24975.
15. Liangtao Zhu, "Adaptive Control of Sinusoidal Brushless DC Motor Actuators," Masters Dissertation, Michigan Tech, 2008, U24986.
16. Petros Ioannou, *Robust Adaptive Control*.
17. Benedict, T.R., and G.W. Bordner, "Synthesis of an Optimal Set of Radar Track-While-Scan Smoothing Functions," *IRE Trans. on Automatic Control*, July 1962.

8 Appendix: Rotation Command

If the axle is to be rotated θ_{cmd} radians, this needs to be done (i) within a prescribed amount of time, (ii) with a specified degree of smoothness, and (iii) with a radian velocity no greater than a specified limit. These requirements are not mutually independent, however. For structural safety, it is better to think in terms of (iv) maximum angular velocity allowed and (v) maximum angular acceleration allowed since (v) limits the applied current and consequently the applied torque and (vi) limits the total rotational inertia allowed in the system.

With items (v) and (vi) in mind for large angular changes, the methodology outlined in Figure 31 achieves both objectives while being relatively simple. In this figure, the (positive) angular acceleration is limited to $a_{\theta_{max}} = 2a_{\theta} / T_r \text{ rad/sec}^2$ and the radian velocity is limited to $\omega_{max} \text{ rad/sec}$. A computed example¹⁴ is shown in Figure 32.

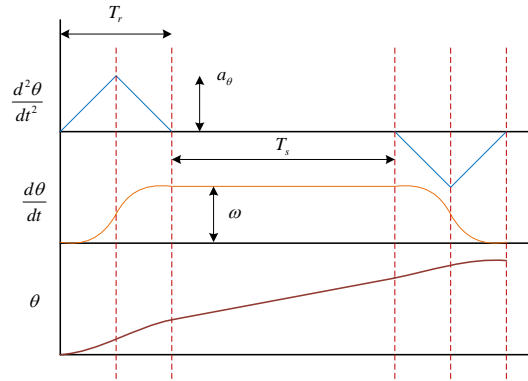


Figure 31 Angular acceleration and angular velocity should be constrained in order to limit the torque required and rotational speed used

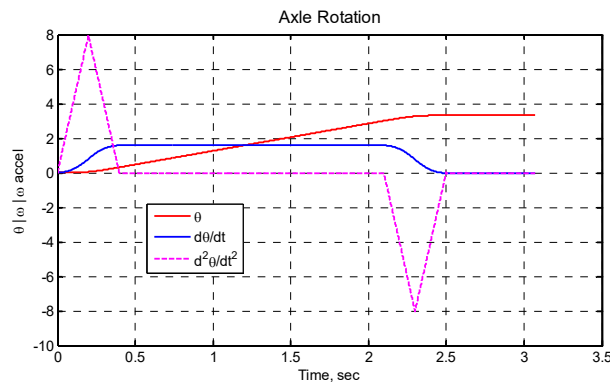


Figure 32 Computed example using the concepts of Figure 31. Maximum radian acceleration limited to 8 rad/sec^2 and maximum radian velocity limited to 1.6 rad/sec . Time required to traverse 4 radian change is about 2.5 sec.

More concisely in the context of Figure 31 and Figure 32, denote the maximum angular acceleration as $a_{\theta_{max}}$. Assuming that the angular rotation is in the positive sense, denote the maximum allowed angular velocity as ω_{max} . From Figure 31,

$$T_{r \min} = \frac{2\omega_{max}}{a_{\theta_{max}}} \quad (25)$$

¹⁴ u25930_rotation_trajectory.m.

For simplicity, the same value of T_r can be used for all cases and it is convenient to simply choose $T_r = T_{r\min}$. In addition,

$$\begin{aligned}
 & \text{if } (\theta_{cmd} > 2\omega_{\max}T_r) \\
 & \quad T_s = \frac{\theta_{cmd}}{\omega_{\max}} - 2T_r \\
 & \quad a_{\theta} = a_{\theta\max} \\
 & \text{else} \\
 & \quad T_s = 0 \\
 & \quad a_{\theta} = \frac{\theta_{cmd}}{2T_r} \\
 & \text{end}
 \end{aligned} \tag{26}$$

where θ_{cmd} is the desired rotation angle change in radians. From the previous two figures, in the case where $T_s \equiv 0$,

$$a(t) = \begin{cases} a_{\theta} & 0 < t \leq \frac{T_r}{2} \\ -a_{\theta} & \frac{T_r}{2} < t \leq \frac{3}{2}T_r \\ a_{\theta} & \frac{3}{2}T_r < t \leq 2T_r \end{cases} \tag{27}$$

and otherwise zero. In the case where $T_s \neq 0$,

$$a(t) = \begin{cases} a_{\theta} & 0 < t \leq \frac{T_r}{2} \\ -a_{\theta} & \frac{T_r}{2} < t \leq T_r \\ -a_{\theta} & T_r + T_s < t \leq T_s + \frac{3}{2}T_r \\ a_{\theta} & T_s + \frac{3}{2}T_r < t \leq T_s + 2T_r \end{cases} \tag{28}$$

but otherwise equal to zero. Given $a(t)$, the radian velocity and angle are given by

$$\begin{aligned}
 \omega(t) &= \int_0^t a(u) du \\
 \theta(t) &= \int_0^t \omega(u) du
 \end{aligned} \tag{29}$$

9 Appendix: Motor Magnetics Fundamentals

The space around a magnet or a current-carrying conductor is the site of a magnetic field \mathbf{B} . The magnetic field vector at any point is related to the magnetic field lines as [5]

- The tangent to a line of \mathbf{B} at any point gives the direction of \mathbf{B} at that point.
- The lines of \mathbf{B} are drawn so that the number of lines per unit cross-sectional area is proportional to the magnitude of the magnetic field vector \mathbf{B} .

The flux Φ_B for a magnetic field over a surface of interest is defined as

$$\Phi_B = \int \mathbf{B} \cdot d\mathbf{S} \quad (30)$$

Consider a positive test charge q_o with an arbitrary velocity vector \mathbf{v} being directed through a point P . The charge will experience a sideways directed force \mathbf{F} in the presence of a magnetic field as shown in Figure 33 given by

$$\mathbf{F} = q_o \mathbf{v} \times \mathbf{B} \quad (31)$$

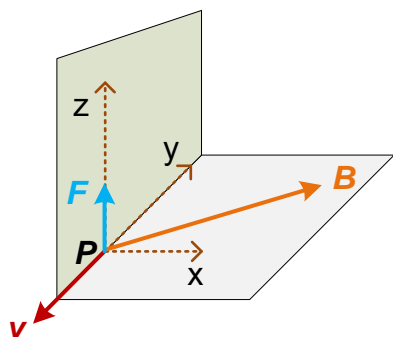


Figure 33 Positive test charge q_o situated at point P with velocity vector \mathbf{v} in the presence of magnetic field \mathbf{B}

The MSK unit associated with \mathbf{B} from (31) is given by

$$\begin{aligned} 1 \text{ tesla} &= \frac{\left(\frac{\text{newton}}{\text{coulomb}} \right)}{\left(\frac{\text{meter}}{\text{sec}} \right)} = \frac{\text{newton sec}}{\text{coulomb meter}} \\ &= \frac{\text{weber}}{\text{meter}^2} = 10^4 \text{ gauss} \\ &= \frac{\text{newton}}{\text{ampere meter}} \end{aligned} \quad (32)$$

The unit of measure used for magnetic flux Φ_B is the weber.

It is important to note that since the magnetic force is always at right angles to the direction of motion, no work is performed on the charged particle. Consequently, a static magnetic field cannot change the kinetic energy of a moving charge; only deflect its trajectory sideways.

From Ampere's law, the relationship between an electrical current i and its associated magnetic field is given by

$$\oint \mathbf{B} \cdot d\mathbf{l} = \mu_o i \quad (33)$$

where the permeability constant of free space is represented by $\mu_o = 4\pi 10^{-7} \frac{\text{weber}}{\text{amp meter}}$. The direction

of the current relative to the current is given by the "right hand rule." Grasp the wire with the right hand, the thumb pointing in the direction of the current. The fingers will curl around the wire in the direction of \mathbf{B} [5].

9.1 Two Parallel Conductors

The magnetic lines of \mathbf{B} are shown for a long current-carrying wire immersed in a uniform external field \mathbf{B}_e in Figure 34. The electrical current is flowing perpendicularly out of the page. Applying the right-hand rule, the magnetic files associated with the current oppose the external magnetic field lines above the wire whereas they reinforce (add to) the external field lines below the wire. This higher concentration of magnetic lines is shown as more closely-spaced field lines below the wire in the figure.

A case of two parallel conductors carrying currents is shown in Figure 35. Based upon (31), it can be shown that each wire will experience a sideways force \mathbf{F} (wires will be attracted to each other) given by

$$\mathbf{F} = i\mathbf{l} \times \mathbf{B} \quad (34)$$

where i is the value of electrical current and \mathbf{l} is a unit-vector in the direction of current flow.

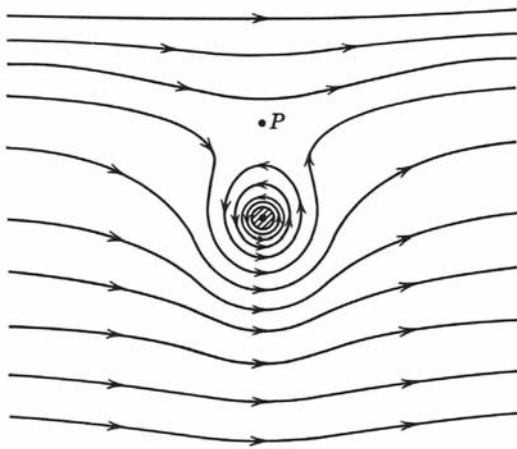


Figure 34 Lines of \mathbf{B} near a long current-carrying wire¹⁵ immersed in a uniform external field \mathbf{B}_e

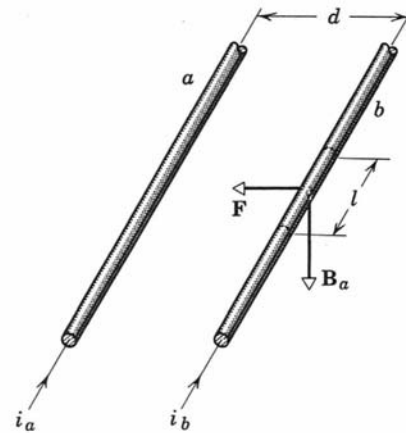


Figure 35 Two parallel wires that carry parallel currents attract each other¹⁶

I am reminded of a Youtube video (<https://www.youtube.com/watch?v=vAs9EHtKfVc>) in which some hackers constructed a rail gun using banks of capacitors to provide extremely high peak-current to power their gun. In their case, they had the heavy gauge cables running to and from the gun (oppositely-directed currents) situated relatively close to each other and parallel to each other. When the rail gun was shot, the huge electrical currents caused opposing forces in the heavy-gauge cables thereby ripping them off the gun connections and throwing the cables apart as shown in Figure 36 and Figure 37. This was completely unexpected by the hackers; just one more example about being knowledgeable when dealing with large amounts of energy in advance!

Returning to (34) in the context of Figure 35, the force exerted on wire b lies in the plane of the two wires and points to the left in the figure with a force per unit length of

$$\left(\frac{\mathbf{F}_b}{l} \right) = i_a \mathbf{B}_a = \frac{\mu_0 i_a i_b}{2\pi d} \quad (35)$$

where d is the distance between the two wires.

¹⁵ Figure 30-7 from [5].

¹⁶ Figure 30-8 from [5].

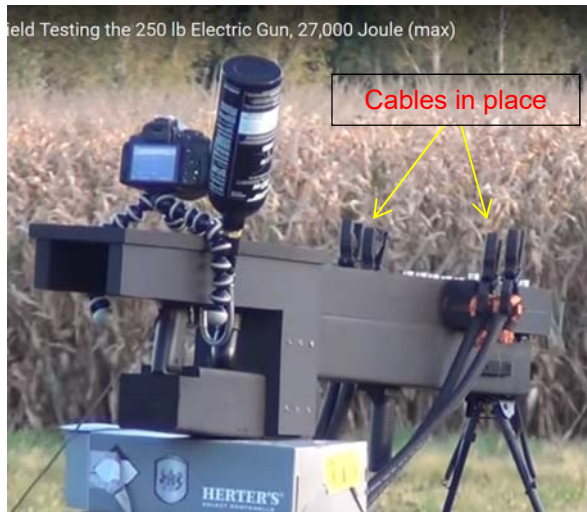


Figure 36 Immediately before the rail gun shot



Figure 37 Milliseconds after the shot with power cables flying

Two comments pertaining to (35) can be offered. When winding a coil, the turns are wound in the same direction (clock-wise or counter-clock-wise). When current is passed through the coil, the wire turns will be attracted to each other because the currents are flowing parallel to each other which draws the turns of wire closer together rather than trying to force them apart. Secondly, the magnitude of the attractive force can be greatly increased if a ferrous material is used as a core thereby replacing μ_o with $\mu_o\mu_r = \mu$.

9.2 Faraday's Law

$$V_{emf} = -\frac{\partial\Phi}{\partial t} \quad (36)$$

10 Appendix: Clarke and Park Coordinate Transformations

The mathematical discussion of 3-phase motors is simplified appreciably if several relatively simple coordinate transformations are employed. This is generally the adopted approach as described in [3].

A plot of the three traditional 3-phase voltage waveforms is shown in Figure 38. The voltages can be expressed mathematically as

$$\begin{aligned} V_a(t) &= A_o \cos(\omega t) \\ V_b(t) &= A_o \cos\left(\omega t + \frac{2\pi}{3}\right) \\ V_c(t) &= A_o \cos\left(\omega t - \frac{2\pi}{3}\right) \end{aligned} \quad (37)$$

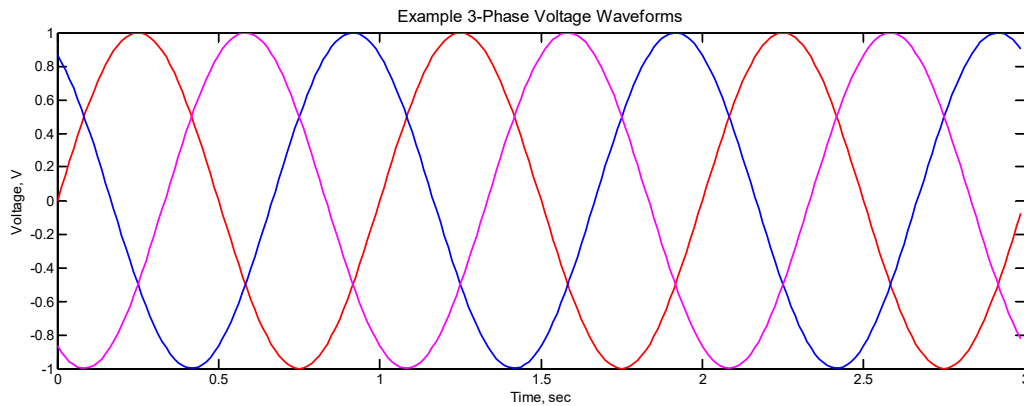


Figure 38 Example of 3-phase voltage waveform having a 1 second period and phases each separated by $2\pi/3$ radians

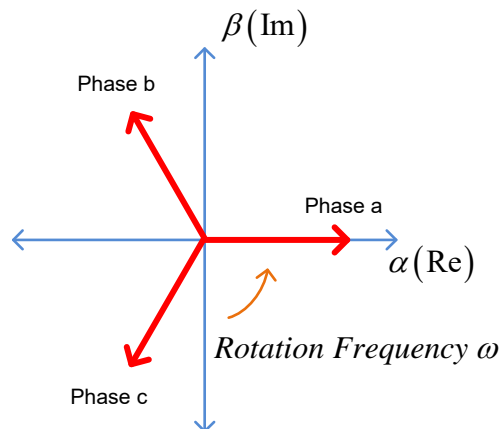


Figure 39 3-phase voltages can be represented by the projection of each phase vector on either the real axis or the imaginary axis

The three phase voltages can also be represented in complex vector form as shown in Figure 39 and mathematically be represented as

$$\begin{aligned}
V_{sa}(t) &= A_o \exp(j\omega t) \\
V_{sb}(t) &= A_o \exp\left(j\omega t + j\frac{2\pi}{3}\right) \\
V_{sc}(t) &= A_o \exp\left(j\omega t - j\frac{2\pi}{3}\right)
\end{aligned} \tag{38}$$

Although there are 3 vectors shown in Figure 39, they are all contained within the single plane (α, β) because they are not linearly independent of one another. The additional subscript on the V 's is purposely intended to show that these are complex vector quantities. For the usual symmetric case,

$$V_{sa}(t) + V_{sb}(t) + V_{sc}(t) = 0 \tag{39}$$

If the sum in (39) is broken into its real and imaginary parts, it can be shown that the resultant sum is equivalent in the new coordinate system to

$$\begin{aligned}
\alpha &= K \left(V_{sa} - \frac{V_{sb}}{2} - \frac{V_{sc}}{2} \right) \\
\beta &= K \left(\frac{\sqrt{3}}{2} V_{sb} - \frac{\sqrt{3}}{2} V_{sc} \right)
\end{aligned} \tag{40}$$

where K is a proportionality constant. Continuing with (39) and (40),

$$\frac{\alpha}{K} = V_{sa} - \frac{V_{sb}}{2} - \frac{V_{sc}}{2} \tag{41}$$

$$0 = \frac{V_{sa}}{2} + \frac{V_{sb}}{2} + \frac{V_{sc}}{2} \tag{42}$$

and summing the two equations leads to

$$\frac{\alpha}{K} = \frac{3}{2} V_a \tag{43}$$

It proves advantageous to choose $\alpha = V_a$ thereby resulting in $K = 2/3$. Using this result in (40) finally leads to the Clarke transformation given by

$$\begin{bmatrix} V_\alpha \\ V_\beta \end{bmatrix} = \begin{bmatrix} \frac{2}{3} & -\frac{1}{3} & -\frac{1}{3} \\ 0 & \frac{1}{\sqrt{3}} & -\frac{1}{\sqrt{3}} \end{bmatrix} \begin{bmatrix} V_{sa} \\ V_{sb} \\ V_{sc} \end{bmatrix} \tag{44}$$

Note that the (α, β) coordinate system is still rotating with angular velocity ω .

Parallel relationships apply to the phase currents as well. Specifically,

$$\begin{bmatrix} i_\alpha \\ i_\beta \end{bmatrix} = \begin{bmatrix} \frac{2}{3} & \frac{-1}{3} & \frac{-1}{3} \\ 0 & \frac{1}{\sqrt{3}} & \frac{-1}{\sqrt{3}} \end{bmatrix} \begin{bmatrix} i_{sa} \\ i_{sb} \\ i_{sc} \end{bmatrix} \quad (45)$$

It is interesting to compute one power-related quantity as

$$P_{\alpha\beta} = V_\alpha i_\alpha^* + V_\beta i_\beta^* \quad (46)$$

where the asterisk denotes complex conjugation. Making the appropriate substitutions,

$$\begin{aligned} P_{\alpha\beta} &= \left(\frac{2}{3} V_{sa} - \frac{1}{3} V_{sb} - \frac{1}{3} V_{sc} \right) \left(\frac{2}{3} i_{sa}^* - \frac{1}{3} i_{sb}^* - \frac{1}{3} i_{sc}^* \right) + \left(\frac{1}{\sqrt{3}} V_{sb} - \frac{1}{\sqrt{3}} V_{sc} \right) \left(\frac{1}{\sqrt{3}} i_{sb}^* - \frac{1}{\sqrt{3}} i_{sc}^* \right) \\ &= \frac{2}{3} (V_{sa} i_{sa}^* + V_{sb} i_{sb}^* + V_{sc} i_{sc}^*) \end{aligned} \quad (47)$$

10.1 Park Transformation

The stator quantities in the (α, β) coordinate system can be simplified further by transforming them into the d - q coordinate system using the Park transformation. This transformation breaks the stator currents into torque- (i_{sq}) and flux- (i_{sd}) producing components thereby allowing each quantity to be controlled independently. This is done by first establishing the d - q coordinate system as

$$\Psi_M = \sqrt{\Psi_{M\alpha}^2 + \Psi_{M\beta}^2} \quad (48)$$

$$\sin(\phi_{field}) = \frac{\Psi_{M\beta}}{\Psi_M} \quad (49)$$

$$\cos(\phi_{field}) = \frac{\Psi_{M\alpha}}{\Psi_M}$$

With the magnetic field angle ϕ_{field} known, the transform from (α, β) to (d, q) coordinates is given by

$$\begin{bmatrix} d \\ q \end{bmatrix} = \begin{bmatrix} \cos(\phi_{field}) & \sin(\phi_{field}) \\ -\sin(\phi_{field}) & \cos(\phi_{field}) \end{bmatrix} \begin{bmatrix} \alpha \\ \beta \end{bmatrix} \quad (50)$$

11 Appendix: State-Variable System Representation

The control system shown in Figure 27 is complicated compared to most traditional control system discussions, having a total of 9 state-variables involved. This level of complexity warrants treatment using the state-variable method.

Although Figure 27 is complicated and involves on the order of ten state variables, the system has only one input θ_{cmd} , one input disturbance (the encoder quantization noise), and one output (the true angular position of the motor). As such, the set of describing differential equations can be written as

$$\frac{d}{dt} \vec{x} = F \vec{x} + Gu + G_1 w \quad (51)$$

where \vec{x} is the system state, $u = \theta_{cmd}$, and w is the encoder quantization noise. The homogenous solution to (51) is given by

$$\vec{x}_h(t) = \exp[F(t-t_o)] \vec{x}(t_o) \quad (52)$$

As such,

$$\exp[F(t-t_o)] = \sum_{k=0}^{\infty} F^k \frac{(t-t_o)^k}{k!} \quad (53)$$

In the case when $u \neq 0$, the particular solution to (51) can be found using variation of parameters as

$$\vec{x}_p(t) = \exp[F(t-t_o)] \vec{v}(t) \quad (54)$$

Upon substitution into (51) (with $w = 0$), it can be shown that

$$\frac{d}{dt} \vec{v}(t) = \exp[-F(t-t_o)] Gu \quad (55)$$

thereby leading to

$$\vec{x}_p(t) = \int_{t_o}^t \exp[F(t-\tau)] Gu(\tau) d\tau \quad (56)$$

The complete solution for the discrete-time case follows as

$$\vec{x}(nT_s + T_s) = \exp[FT_s] \vec{x}(nT_s) + \int_{nT_s}^{(n+1)T_s} \exp[F(nT_s + T_s - \tau)] Gu(\tau) d\tau \quad (57)$$

12 Appendix: Control System Design

Once the motor has been adequately characterized, the control law details in terms of the sampling-rates and gain terms in Figure 27 must be found. For lower-order systems, methods like Ackermann's formula may be employed but a more sophisticated approach is needed for systems having the complexity of Figure 27.

MATLAB has a wealth of functions specifically designed to assist with control system design.

The control loop configuration shown in Figure 27 is not, however, in an easily manageable form like that stipulated in (51) of §11. But it can be transformed into a more appropriate form as shown in (58). Some simplifications have been incorporated, however. First of all, the products involving ω_{est} in (24) would be nonlinear cross-products between state variables, so the approximation $\omega_{est} \approx 0$ has been used. Secondly (58) does not include the observer details yet, so $\theta_{est} = \theta_m$ and $\omega_{est} = \omega_m$ have been tentatively made.

One of the more important aspects of this exercise is the reduction of Figure 27 into the traditional state-space description $d\vec{x}/dt = A\vec{x} + B\vec{\mu}$. The gain-term products appearing in the A matrix motivate using a simplified construction where single-variable gain entries are sufficient.

$$\frac{d}{dt} \begin{bmatrix} i_d \\ i_q \\ \omega_m \\ \theta_m \\ \omega_{est} \\ \theta_{est} \\ sv_1 \\ sv_2 \\ sv_3 \end{bmatrix} = \begin{bmatrix} -1/\tau & 0 & 0 & 0 & 0 & 0 & 0 & 0 & k_{id2} \\ 0 & -k_{iq1} - 1/\tau & -\Psi_M/L & 0 & -k_{iq1}k_{w1} & -k_{iq1}k_{w1}k_{ph} & k_{iq1}k_{w2} & k_{iq2} & 0 \\ 0 & 3p^2\Psi_M/2J & -K_f/J & 0 & 0 & 0 & 0 & 0 & 0 \\ 0 & 0 & 1 & 0 & 0 & 0 & 0 & 0 & 0 \\ 0 & 0 & 1 & 0 & 0 & 0 & 0 & 0 & 0 \\ 0 & 0 & 0 & 1 & 0 & 0 & 0 & 0 & 0 \\ 0 & 0 & 0 & 0 & -1 & k_{ph} & 0 & 0 & 0 \\ 0 & -1 & 0 & 0 & -k_{w1} & -k_{w1}k_{ph} & k_{w2} & 0 & 0 \\ -1 & 0 & 0 & 0 & 0 & 0 & 0 & 0 & 0 \end{bmatrix} \begin{bmatrix} i_d \\ i_q \\ \omega_m \\ \theta_m \\ \omega_{est} \\ \theta_{est} \\ sv_1 \\ sv_2 \\ sv_3 \end{bmatrix} + \begin{bmatrix} i_{d,cmd}k_{id1}/L \\ k_{iq1}k_{w1}k_{ph}\theta_{cmd} \\ -p\tau_{load}/J \\ 0 \\ 0 \\ 0 \\ k_{ph}\theta_{cmd} \\ k_{w1}k_{ph}\theta_{cmd} \\ i_{d,cmd} \end{bmatrix} \quad (58)$$

This project installment is already quite lengthy, so the design details will be deferred until the next installment. The next installment will include:

- Simplification of Figure 27 to expressly omit products between gain terms
- Investigation into controllability and observability aspects of the system
- Use of transformation methods to further reduce the design to a canonical form
- Invocation of *optimal control theory* to complete the control system design

Stay tuned.

13 Appendix: Associated Equipment

I have owned a large format CNC router for some time as shown here in Figure 40. The center hub shown in Figure 12 through Figure 16 was fabricated on this machine.

Since most of my optics-related work will entail circular symmetry of some kind, I acquired the used LG1440 Supermax lathe shown in Figure 41 in late 2018. This lathe is completely manual primarily because I wanted to put most of my project dollars into the purchase of a serious mill. The LG1440 comes in at about 1800 pounds.

In late 2018, I also acquired a new Haas TM1P milling machine as shown in Figure 42. This machine is quite a step up from my original CNC router shown in Figure 40! This machine has (x, y, z) travels of 30", 12", and 16". It can handle a workpiece weighing up to 1,000 pounds. The milling precision is on the order of 0.0002" (about 5 μm). This is a full CNC machine, but its front panel offers a wide range of capabilities making it possible to function as almost a manual mill. Views along the x-axis and y-axis within the machine are shown in Figure 44 and Figure 43 respectively.

One of the smarter albeit expensive options I purchased with the TM1P was the Renishaw wireless probing option. This option makes it possible to assess tool and workpiece offsets very quickly and with maximum precision. When milling both sides of a workpiece, for instance, this probing option makes it almost trivial to realign the workpiece in all three dimensions with the same degree of precision. The Renishaw tool probe is shown in Figure 45 with the workpiece probe shown in Figure 46.

The initial learning curve for the new lathe and CNC mill has taken most of my discretionary time since last November. Coming up to speed with the TM1P mill not only entailed getting familiar with the machine itself, but also adopting a completely new CAD tool (Fusion 360).

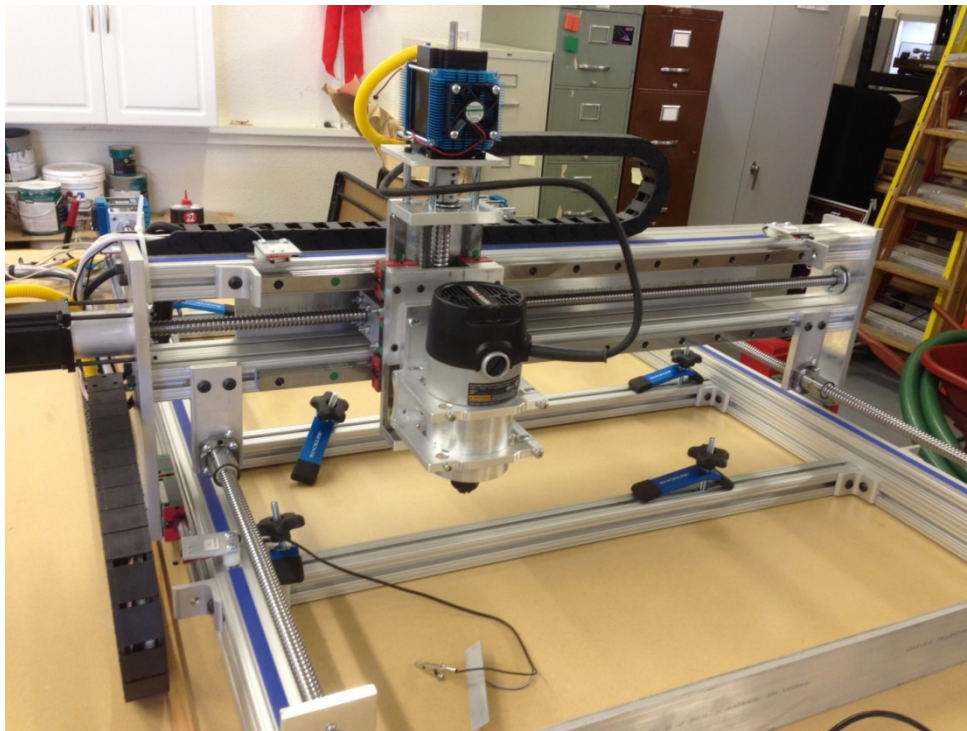


Figure 40 CNC router. With the Haas mill acquisition (Figure 42), the long-term plan will likely be to replace the router head with a 3-D printing head.



Figure 41 LG1440 metal lathe acquired November 2018



Figure 42 Haas TM-1P CNC vertical milling machine acquired December 2018. Machine precision is specified at 0.0002" (5.1 μm) and the table can support a workpiece weighing up to 1,000 pounds. The automatic tool changer combined with the Renishaw probing system make precision tool and workpiece alignment a breeze.



Figure 43 Looking down along the y-axis in the TM1P mill

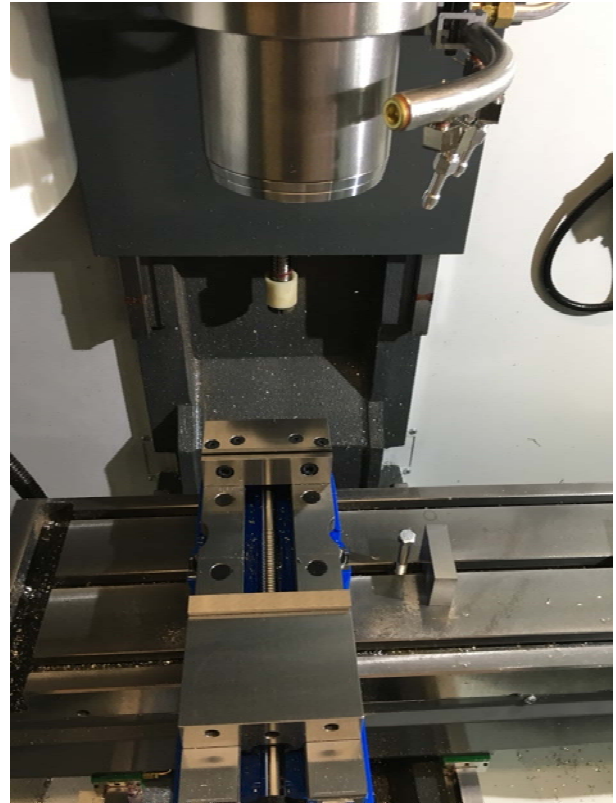


Figure 44 Looking under the mill's spindle along the x-axis



Figure 45 Precision Renishaw tool probe

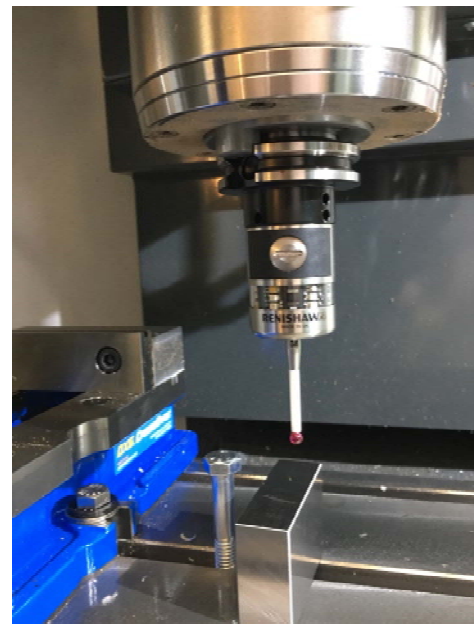


Figure 46 Precision Renishaw workpiece probe